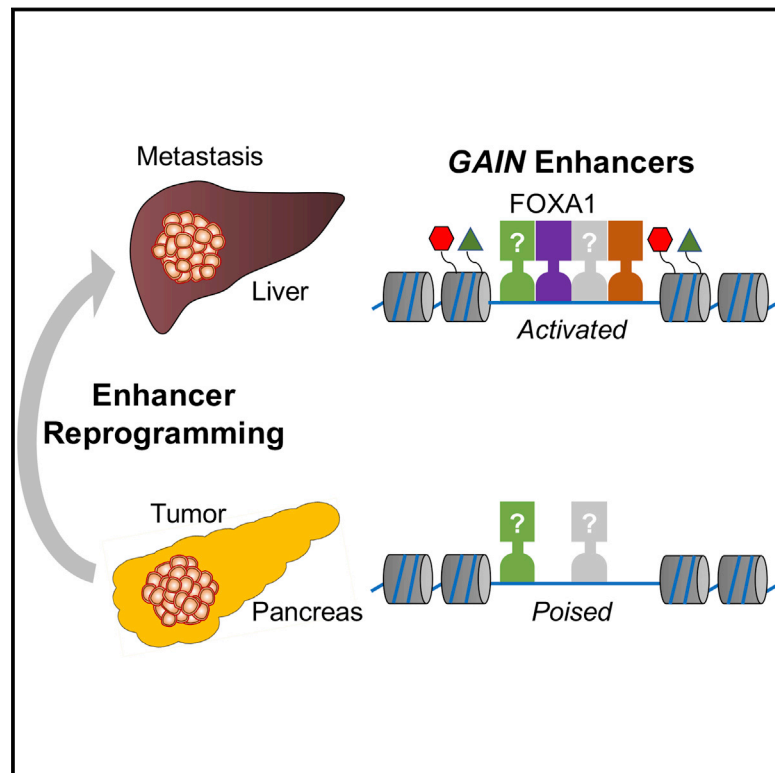


Enhancer Reprogramming Promotes Pancreatic Cancer Metastasis

Graphical Abstract



Authors

Jae-Seok Roe, Chang-Il Hwang, Tim D.D. Somerville, ..., Youngkyu Park, David A. Tuveson, Christopher R. Vakoc

Correspondence

dtuveson@cshl.edu (D.A.T.), vakoc@cshl.edu (C.R.V.)

In Brief

Large-scale enhancer reprogramming directed by transcription factors such as FOXA1 drives metastasis in the organoid model of pancreatic cancer.

Highlights

- Recurrent changes in enhancer activity are associated with PDA metastasis
- FOXA1 drives enhancer reprogramming during PDA progression
- Manipulation of FOXA1 in PDA cells alters enhancer activity and disease aggressiveness
- FOXA1 drives an aberrant developmental transition in PDA toward embryonic endoderm



Enhancer Reprogramming Promotes Pancreatic Cancer Metastasis

Jae-Seok Roe,^{1,9} Chang-Il Hwang,^{1,2,9} Tim D.D. Somerville,¹ Joseph P. Milazzo,¹ Eun Jung Lee,^{1,2} Brandon Da Silva,^{1,2} Laura Maiorino,¹ Hervé Tiriach,^{1,2} C. Megan Young,^{1,2} Koji Miyabayashi,^{1,2} Dea Filippini,^{1,2} Brianna Creighton,^{1,2} Richard A. Burkhardt,³ Jonathan M. Buscaglia,⁴ Edward J. Kim,⁵ Jean L. Grem,⁶ Audrey J. Lazenby,⁷ James A. Grunkemeyer,⁸ Michael A. Hollingsworth,⁸ Paul M. Grandgenett,⁸ Mikala Egeblad,¹ Youngkyu Park,^{1,2} David A. Tuveson,^{1,2,*} and Christopher R. Vakoc^{1,10,*}

¹Cold Spring Harbor Laboratory, Cold Spring Harbor, NY 11724, USA

²Lustgarten Foundation Pancreatic Cancer Research Laboratory, Cold Spring Harbor, NY 11724, USA

³Division of Hepatobiliary and Pancreatic Surgery, Department of Surgery, Johns Hopkins Hospital, Baltimore, MD 21287, USA

⁴Division of Gastroenterology & Hepatology, Stony Brook University School of Medicine, Stony Brook, NY 11790, USA

⁵Division of Hematology/Oncology, UC Davis Medical Center, Sacramento, CA 95817, USA

⁶Department of Medicine, University of Nebraska Medical Center, Omaha, NE 68198, USA

⁷Department of Pathology and Microbiology, University of Nebraska Medical Center, Omaha, NE 68198, USA

⁸Eppley Institute for Research in Cancer and Allied Diseases, Fred & Pamela Buffett Cancer Center, University of Nebraska Medical Center, Omaha, NE 68198, USA

⁹These authors contributed equally

¹⁰Lead Contact

*Correspondence: dtuveson@cshl.edu (D.A.T.), vakoc@cshl.edu (C.R.V.)

<http://dx.doi.org/10.1016/j.cell.2017.07.007>

SUMMARY

Pancreatic ductal adenocarcinoma (PDA) is one of the most lethal human malignancies, owing in part to its propensity for metastasis. Here, we used an organoid culture system to investigate how transcription and the enhancer landscape become altered during discrete stages of disease progression in a PDA mouse model. This approach revealed that the metastatic transition is accompanied by massive and recurrent alterations in enhancer activity. We implicate the pioneer factor FOXA1 as a driver of enhancer activation in this system, a mechanism that renders PDA cells more invasive and less anchorage-dependent for growth in vitro, as well as more metastatic in vivo. In this context, FOXA1-dependent enhancer reprogramming activates a transcriptional program of embryonic foregut endoderm. Collectively, our study implicates enhancer reprogramming, FOXA1 upregulation, and a retrograde developmental transition in PDA metastasis.

INTRODUCTION

Pancreatic ductal adenocarcinoma (PDA) is the fourth leading cause of cancer deaths in the United States, owing in part to its early onset of metastasis. Most PDA patients will already have metastases at the time of diagnosis, a point in which surgical or chemotherapeutic interventions have minimal benefit (Ryan et al., 2014). Consequently, the prognosis for PDA patients is dismal, with only 8% of patients surviving more than 5 years after diagnosis (Siegel et al., 2017). One obstacle underlying

these clinical challenges is our limited understanding of molecular mechanisms of PDA metastasis, in particular with regard to the origin of metastatic traits.

Unlike the deep understanding of mutational mechanisms that initiate PDA, a genetic basis for metastasis in this disease is unclear. The initiating genetic event in most PDA patients is an activating mutation of *KRAS* in an acinar or ductal cell, which is sufficient to initiate a pre-malignant (also known PanIN; pancreatic intraepithelial neoplasia) lesion of disorganized epithelial architecture. Subsequent inactivating mutations of tumor suppressor genes (e.g., *TP53*) are sufficient to drive tumor formation at the primary site, a finding supported by genetically engineered mouse models (GEMMs) of PDA (Guerra and Barbacid, 2013). In contrast, a recurrent metastasis-specific mutation has yet to be identified (Campbell et al., 2010; Makohon-Moore et al., 2017; Yachida et al., 2010). It has been proposed that fluctuations of gene expression or signal transduction among cells within the primary tumor are critical for the acquisition of metastatic potential (Neureiter et al., 2014). Candidate metastasis-promoting mechanisms include signaling cues from the tumor microenvironment, as well as pathways regulating self-renewal and epithelial-to-mesenchymal transitions (EMT) (Kong et al., 2011; Krebs et al., 2017; Öhlund et al., 2014).

Alteration of epigenetic pathways is an emerging mechanism of PDA progression. Whole-genome sequencing studies have identified inactivating mutations of chromatin modifiers as frequent genetic events in PDA tumors (Waddell et al., 2015). In addition, small molecules that target readers, writers, or erasers of histone modifications have shown promising therapeutic effects in mouse models of PDA by altering transcription of cancer genes (Hessmann et al., 2017). A recent study has shown that disruption of large heterochromatin domains is associated with the metastatic transition in PDA as a consequence of aberrant oxidative pentose phosphate metabolism (McDonald

et al., 2017). However, the direct functional evidence that links chromatin regulation to PDA metastasis remains limited.

Enhancers are a class of regulatory DNA elements composed of clusters of transcription factor (TF) binding sites, which are uniquely capable of stimulating transcription over large genomic distances (Spitz and Furlong, 2012). At enhancers, TFs trigger the recruitment of chromatin-modifying enzymes to establish a stereotypical pattern of covalent histone modifications on adjacent nucleosomes, such as histone H3 lysine 27 acetylation (H3K27ac) and histone H3 lysine 4 mono-methylation (H3K4me1) (Long et al., 2016). As a result, genome-wide measurements of H3K27ac and H3K4me1 enrichment using chromatin immunoprecipitation (ChIP-seq) or chromatin accessibility (e.g., using the assay for transposase-accessible chromatin [ATAC-seq]) allow for the annotation of active enhancer landscapes in different cellular states (Yue et al., 2014). One study has applied ChIP-seq analysis to human PDA cell lines to expose enhancer profiles and TFs that correlate with the degree of epithelial differentiation, or disease “grade” (Diaferia et al., 2016). However, it has yet to be determined how the enhancer landscape evolves during each stage of PDA progression.

We recently developed an organoid culture model of PDA, which preserves the unique biological characteristics of normal, PanIN, tumor, and metastatic lesions and allows for direct biochemical comparisons during each stage of disease progression (Boj et al., 2015; Chio et al., 2016). Here, we used this system to characterize how the enhancer landscape evolves during PDA progression and identified dramatic changes in enhancer activity associated with metastasis. We implicate the developmental TF FOXA1 in promoting aberrant enhancer activation in this setting, which we show can promote metastatic phenotypes in vivo. Collectively, our findings suggest that reprogramming of the enhancer landscape can promote the acquisition of metastatic traits.

RESULTS

Paired Tumor- and Metastasis-Derived Organoids Provide a Model to Study Mechanisms of PDA Progression

We previously demonstrated that normal and neoplastic pancreatic ductal cells can be cultured as organoids, which retain the attributes of the stage of PDA from which they were derived when re-introduced into mice (Boj et al., 2015). We hypothesized that epigenomic comparisons of organoid cultures might reveal mechanisms that promote PDA progression. To carry out this study, we expanded our collection of pancreatic organoids derived from autochthonous primary tumors (T) and paired metastases (M) from the KPC (*Kras*^{+LSL-G12D}; *Trp53*^{+LSL-R172H}; *Pdx1-Cre*) GEMM of PDA (Figure 1A). Matched primary tumor and metastatic lesions were excised from the liver, peritoneum, or diaphragm of six independent KPC mice, and organoids were prepared (Figures 1B and S1A). Consistent with our prior observations, all of the M organoids have lost the remaining wild-type (WT) *Trp53* allele, which is common for disease progression in this system (Figure S1B) (Boj et al., 2015).

We evaluated whether pairs of T and M organoids derived from the same animal retain their respective disease properties when

re-transplanted into mice. When injected orthotopically into the pancreas, a single-cell suspension of M organoids formed macroscopic tumors within 4 weeks associated with metastatic spread, whereas T organoids required 3–4 months to form PDA with metastases (Figure S1C). In addition, when injected into the tail vein of mice, cells from M organoids readily colonized the lung parenchyma within 9 weeks, whereas cells from T organoids lacked this capability (Figures 1C, 1D, and S1D). After portal vein or intra-splenic injection, M organoid cells colonized the liver more efficiently than T organoid cells and grew more readily when injected into the peritoneal wall and subcutaneous space (Figures 1E–1H and S1E–S1H). Collectively, these findings indicate that M organoids have evolved to a more aggressive state than their paired T organoids, and hence, comparisons of these cultures might expose mechanisms that promote metastasis.

Epigenomic Analysis of PDA Organoids Identifies Recurrent Changes in Enhancer Activity Associated with the Metastatic Transition

RNA-seq profiling of the organoid culture series revealed overlapping transcriptional changes to those observed in a prior microarray evaluation of human PDA samples (Moffitt et al., 2015), including upregulation of known regulators of PDA metastasis, *Lin28b*, *Pdgfrb*, and *Runx3* (Figures S2A and S2B) (Kugel et al., 2016; Weissmueller et al., 2014; Whittle et al., 2015). To evaluate how the enhancer landscape becomes altered during PDA progression, we profiled genome-wide enrichment of H3K27ac in organoid cultures derived from two normal pancreatic ducts (hereafter referred to as N), two PanIN lesions (hereafter referred to as P, from the *Kras*^{+LSL-G12D}; *Pdx1-Cre* mice), and the six pairs of T and M organoids described above. We performed a global analysis to identify all genomic intervals with > 10-fold changes in H3K27ac in any of the P, T, or M organoid cultures relative to the N organoids (Figure 2A). While the global level of H3K27ac was similar across these samples, our analysis recovered 857 regions with increased and 1,709 regions with decreased H3K27ac, which we hereafter refer to as *GAIN* and *LOSS* regions, respectively (Figures 2A and S2C). These acetylation changes were almost exclusively identified in the M organoids and occurred in a recurrent manner across the six independent samples, irrespective of the anatomic site of the metastatic lesion (Figures 2B, 2C, and S2C–S2G). An unsupervised hierarchical clustering analysis of global H3K27ac enrichment further supported the epigenomic divergence of M organoids from earlier stages of disease, as well as the convergence of the six M organoids with one another (Figure 2D). This analysis suggests that the metastatic transition in the KPC model is accompanied by dramatic and recurrent changes in H3K27 acetylation.

More than 90% of *GAIN* and *LOSS* regions lie outside of promoter regions and correlate with expression changes of nearby genes, suggesting that they represent enhancer elements (Figures 2E, S2H, and S2I). We focused our subsequent analysis on *GAIN* regions, which we hypothesized might have a role in promoting PDA progression and metastasis. While *GAIN* regions were defined in murine samples, we found that H3K27ac was enriched at the corresponding locations in human PDA cell lines and in patient-derived PDA organoids (Figure S2J). To further

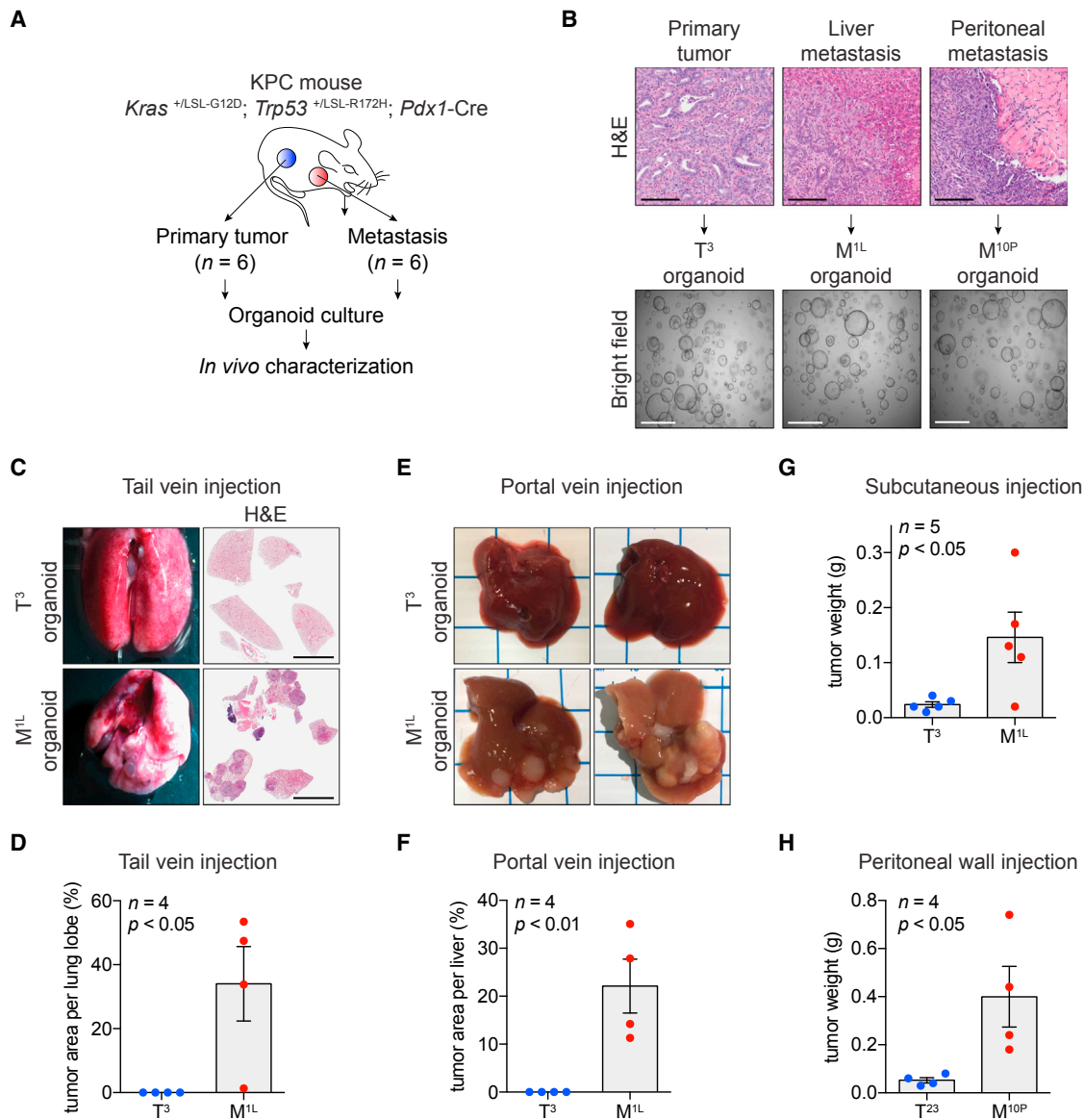


Figure 1. Paired Tumor- and Metastasis-Derived Organoids Provide a Model to Study Mechanisms of PDA Progression

(A) Schematic diagram demonstrating establishment of paired primary tumor- and metastasis-derived organoid cultures from the KPC mouse model of pancreatic cancer.

(B) Hematoxylin and eosin (H&E) staining of murine primary tumor and metastases derived from KPC mice (top) and bright field images of established organoids (bottom). Scale bars, 100 μ m (top) and 1 mm (bottom).

(C and D) Representative bright field images (C, left) and H&E staining (C, right) of lung and quantification (D) 2 months after tail vein injection of T³ and M^{1L} organoids (5×10^5 cells per each injection, $n = 4$) in C57BL/6J mice. Scale bars, 5 mm.

(E and F) Representative bright field images (E) and quantification (F) one month after portal vein injection of T³ and M^{1L} organoids (5×10^5 cells per each injection, $n = 4$) in C57BL/6J mice.

(G) Quantification of subcutaneous tumors 6 weeks after injection of T³ and M^{1L} organoids (5×10^5 cells per each injection, $n = 5$) in C57BL/6J mice.

(H) Quantification of tumor weight 4 weeks after peritoneal wall injection of T²³ and M^{10P} organoids (5×10^5 cells per each injection, $n = 4$) in C57BL/6J mice.

For bar charts, each dot represents a mouse and the mean \pm SEM is shown. p value was determined by Student's t test. See also Figure S1.

validate that *GAIN* regions are active enhancer elements, we profiled two other enhancer-associated chromatin features in three pairs of T and M organoids: H3K4me1 using ChIP-seq and chromatin accessibility using ATAC-seq. As expected, *GAIN* regions were enriched for H3K27ac, H3K4me1, and chro-

matin accessibility in M organoids (Figures 2F and S2K–S2M, red line). While H3K27ac and H3K4me1 were increased when comparing T to M organoids, we noted that chromatin accessibility pre-existed at these sites in all four types of organoids (Figures 2F and S2K). This suggests that *GAIN* regions exist in

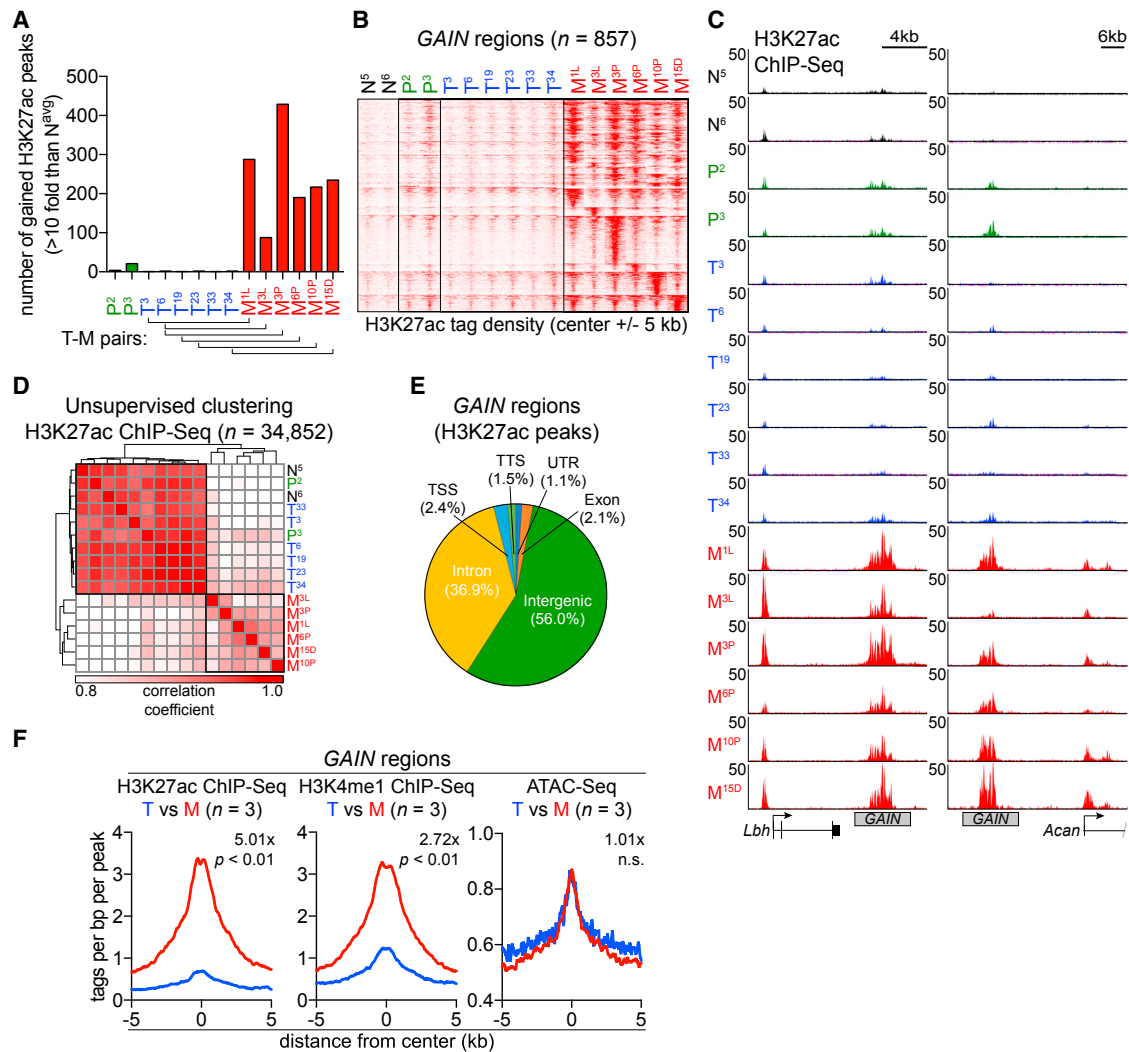


Figure 2. Massive Enhancer Reprogramming Accompanies the Metastatic Transition

(A) Distribution of gained H3K27ac peaks across the indicated P, T, and M organoids. From a total of 34,852 H3K27ac ChIP-seq peaks, gained H3K27ac peaks are defined by more than 10-fold increase of H3K27ac signal relative to the average of N^5 and N^6 (N^{avg}). Bottom brackets indicate the pairs of matching T and M organoids.

(B) Heatmap representation of GAIN regions based on H3K27ac occupancy in organoids. The 857 GAIN regions were identified from the union of all gained H3K27ac peaks described in Figure 2A. 10-Kb around the center of GAIN regions are displayed for each organoid. Each row represents a single region ($n = 857$). Each column represents an individual organoid ($n = 16$).

(C) Representative H3K27ac ChIP-seq profiles of GAIN regions at *Lbh* and *Acan* loci in N, P, T, and M organoids.

(D) Heatmap representation of unsupervised hierarchical clustering based on H3K27ac occupancy at total H3K27ac ChIP-seq peaks. Samples were clustered based on Spearman correlation coefficient with average linkage.

(E) Pie chart showing the genomic annotations of 857 GAIN regions according to the location of a given peak. TSS, “-1-kb to +100-bp” of transcription start sites. TTS, “-100-bp to +1-kb” of transcription termination sites. UTR includes both 5' and 3' UTRs.

(F) Metagene representation of the mean ChIP-seq signal for the indicated histone marks (left and middle) or the mean ATAC-seq signal (right) across GAIN regions in the indicated organoids. Metagenes are centered on the middle of GAIN regions and 10-Kb around the center of GAIN regions are displayed. To compare relative signal changes (denoted as value- x), the mean signal of each biological replicate was determined by averaging signals of 2-Kb (H3K27ac or H3K4me1 ChIP-seq) or 1-Kb (ATAC-seq) around the center of GAIN regions. p value was determined by Kolmogorov-Smirnov test.

See also Figure S2 and Table S1 and S2.

a “poised” state of accessibility in normal ductal cells (Zentgraf and Scacheri, 2012). An ontology analysis of genes located near GAIN regions revealed a significant association with developmental functions, with the most enriched signature being

related to tube development (Figure S2N). While EMT is a known developmental pathway associated with metastasis (Ye and Weinberg, 2015), our RNA-seq analysis did not identify consistent changes in EMT genes (Figure S2O).

Elevated FOXA1 Expression and Occupancy Is Associated with PDA Metastasis and *GAIN* Enhancer Activation

We reasoned that identifying TFs that activate *GAIN* enhancers would allow us to determine whether these *cis* elements are functionally important for PDA metastasis. To this end, we evaluated whether specific TF motifs were enriched within *GAIN* regions using the TRAP algorithm (Thomas-Chollier et al., 2011). The top enriched motifs at *GAIN* regions included binding sites for the AP1, SOX, and Forkhead families of TFs (Figures 3A and S3A). We focused on the Forkhead family TF FOXA1, as we noted in our RNA-seq analysis of organoids that *Foxa1* was upregulated in M organoids, while its homolog *Foxa2* was downregulated (Figures 3B, S3B, and S3C). In addition, we identified a *GAIN* enhancer at the *Foxa1* locus (Figure S3B). In accordance with our motif analysis, ChIP-seq analysis of FOXA1 confirmed its elevated occupancy at *GAIN* regions in M organoids (Figures 3C, 3D, and S3D). An RNA fluorescence in situ hybridization (RNA-FISH) analysis in the KPC mice revealed sporadic regions of focal *Foxa1* upregulation in primary PDA tumors (Figure 3E, white arrows), which became homogeneously upregulated in metastatic lesions (Figure 3E). These findings implicate FOXA1 in *GAIN* enhancer activation.

We next evaluated whether FOXA1 upregulation occurs during human PDA progression. In a prior microarray study of human PDA samples (Moffitt et al., 2015), we identified FOXA1 upregulation in primary tumors, which became further elevated in metastatic lesions ($p < 0.01$) (Figure 3F). We confirmed this overall pattern of FOXA1 upregulation by qRT-PCR analysis of human PDA organoids and by immunohistochemical staining of PDA tissue derived from a rapid autopsy program (Figures S3E–S3G). In addition, levels of FOXA1 expression were correlated with the degree of *GAIN* enhancer activation in human PDA cell lines (Figure S2J) (Diaferia et al., 2016). These results validate that FOXA1 upregulation occurs during human PDA progression.

FOXA proteins are pioneer factors that are essential for the specification of foregut cell fates from primitive endoderm tissues during embryonic development (Figure 3G) (Zaret et al., 2016). Using published datasets, we found that *GAIN* regions and genes became activated during the differentiation of human embryonic stem cells into foregut endoderm (Figures 3H, 3I, S3H, and S3I) (Loh et al., 2014; Xie et al., 2013). These findings raised the possibility that FOXA1 upregulation during PDA progression activates an embryonic foregut endoderm transcriptional program.

FOXA1 Overexpression Promotes *GAIN* Enhancer Activation and Metastasis-Related Phenotypes in Murine and Human PDA Cell Lines

Prior studies have associated low FOXA1 expression with the acquisition of mesenchymal features in PDA cell lines (Diaferia et al., 2016; Song et al., 2010). However, no study to date has evaluated the functional consequences of FOXA1 upregulation in PDA. We initially investigated this in vitro using a 2D cell line derived from a T organoid (hereafter referred to as KPC-2D cells), which allowed us to perform in vitro assays of metastatic potential. Adaptation of T organoids to 2D cultures selects for cells with loss of the WT *Trp53* allele (Boj et al., 2015), as well as

for modest increases in FOXA1 expression and H3K27ac enrichment at *GAIN* regions (Figures S4A and S4B). However, CRISPR-based inactivation of *Trp53* in T organoids was insufficient to cause FOXA1 upregulation and *GAIN* enhancer activation, indicating that p53 loss and enhancer reprogramming occur independently during PDA progression (Figures S4C–S4G).

Since *GAIN* enhancers in KPC-2D cells exist in a partially activated state, we evaluated whether these elements could be fully activated by FOXA1 overexpression. Retroviral transduction of KPC-2D cells with the FOXA1 cDNA led to disproportionately increased FOXA1 occupancy and H3K27ac at *GAIN* regions (Figures 4A, 4B, and S4H). RNA-seq analysis showed that FOXA1 expression caused an increase in the expression of *GAIN* genes and of a foregut endoderm gene signature (Figure 4C). When cultured as a 2D monolayer, we found that FOXA1 expression had no effect on cell proliferation, clonogenic growth, or cell migration (Figures S4I–S4K). However, when cultured as tumor spheres on ultra-low adhesion plates, FOXA1 expression enhanced anchorage-independent growth (Figure 4D). FOXA1-overexpressing KPC-2D cells were also more invasive when placed in Matrigel-coated Boyden chamber assays (Figure 4E). When injected via tail vein into recipient mice, FOXA1 also enhanced the ability of KPC-2D cells to colonize the lung parenchyma (Figure 4F). We observed enhanced tumor sphere formation when overexpressing FOXA1 in human PDA cell lines, which paralleled an increase in H3K27ac at *GAIN* regions and transcriptional activation of foregut development genes (Figures 4G–4J and S4L). These results show that FOXA1 overexpression in PDA cell lines promotes *GAIN* enhancer activation and the acquisition of metastatic phenotypes.

FOXA1-Mediated Enhancer Reprogramming Promotes PDA Progression in an Organoid Transplantation Model

We next considered whether FOXA1 upregulation was sufficient for the entirety of *GAIN* enhancer activation observed in M organoids. To this end, we retrovirally overexpressed FOXA1 in two independent T organoids (T^3 and T^{23}) and carried out H3K27ac ChIP-seq. We observed that FOXA1 expression only elevated H3K27ac to ~25% of the level observed in matched M organoids (Figures 5A, 5B, and S5A). This result led us to search for other candidate TFs that might cooperate with FOXA1 to promote enhancer activation. Our TRAP analysis of FOXA1 peaks and *GAIN* regions revealed an association with motifs recognized by GATA5, BATF2, PRRX2, and PAX9, which are each upregulated at the transcriptional level in M organoids and to varying degrees in human PDA samples (Figures S3A and S5B–S5D). We also found that *LOSS* regions were enriched for a motif recognized by ONECUT1, which is transcriptionally silenced during PDA progression (Figures S5E–S5G) (Moffitt et al., 2015). While overexpressing GATA5, BATF2, PRRX2, or PAX9 in KPC-2D cells each led to enhanced invasiveness in vitro (Figure S5H), we focused on GATA5, since this TF is similar to FOXA1 in being upregulated during both endoderm development and PDA progression (Figures S5I and S5J). GATA5 overexpression in KPC-2D cells led to enhanced clonogenic growth and lung colonization (Figures S5K and S5L). The *Gata5* locus also acquired a *GAIN* enhancer in M organoids (Figure S3B).

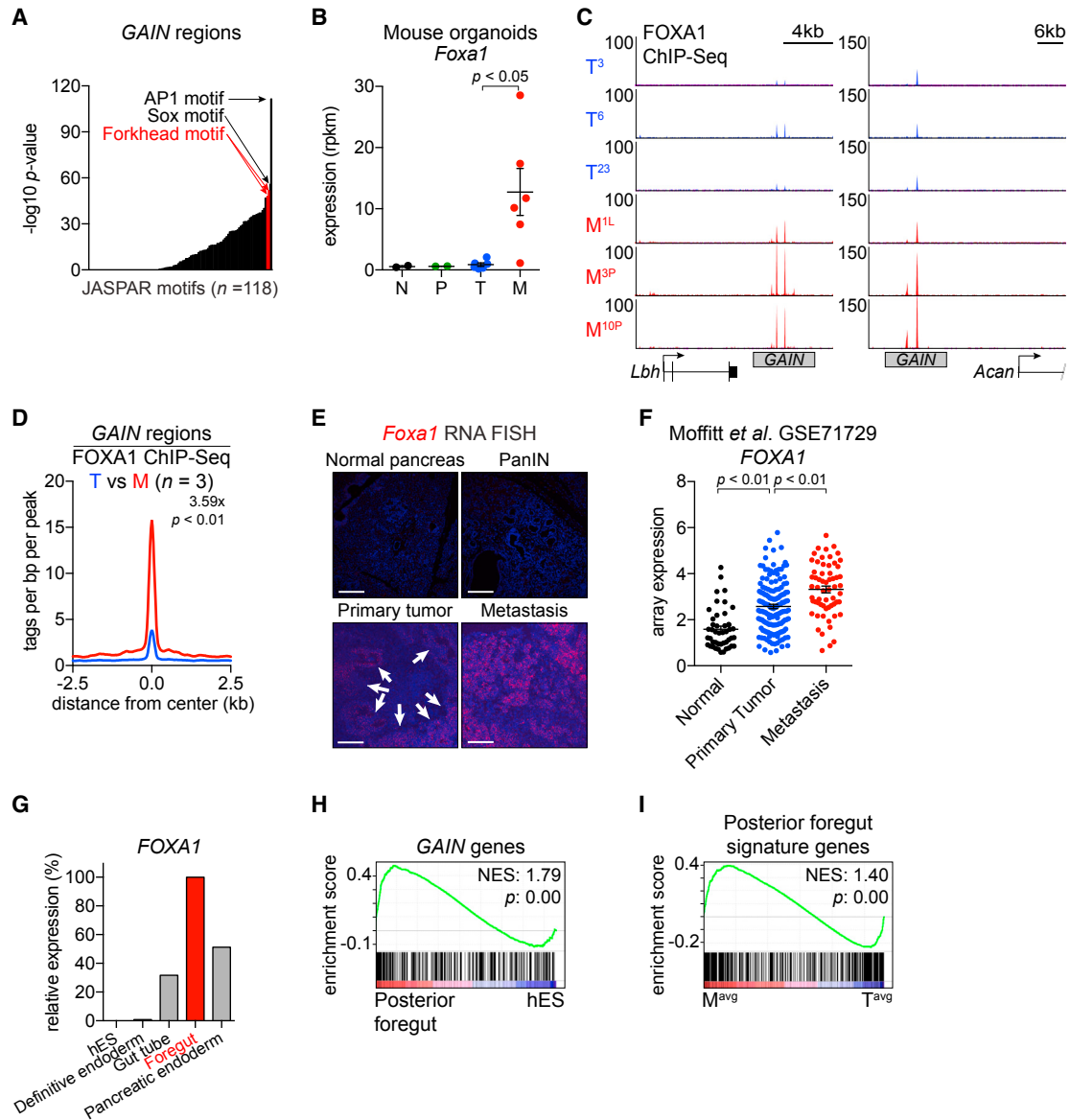


Figure 3. Elevated FOXA1 Expression and Occupancy Are Associated with PDA Metastasis and *GAIN* Enhancer Activation

(A) Representation of motifs enriched at *GAIN* regions. Mouse promoters were used as the comparison library. *p* values correspond to the corrected *p* in the output. AP1 motif is ranked first; SOX motif is ranked second; FOXD1 and FOXA2 motifs are ranked third and fourth, respectively. Position weight matrices for FOXD1 and FOXA2 are represented as Forkhead motifs.

(B) RNA-seq based *Foxa1* mRNA expression in organoids. Each dot represents an independent organoid culture, and the mean \pm SEM is shown. *p* value was determined by Student's *t* test. N, normal; P, PanIN; T, primary tumor; M, metastasis; rpkm, reads per kilobase per million mapped reads.

(C) Representative FOXA1 ChIP-seq profiles of *GAIN* regions at *Lbh* and *Acan* loci in the indicated organoids.

(D) Metagenome representation of the mean FOXA1 ChIP-seq signal across *GAIN* regions in the indicated organoids. The mean signal of each biological replicate was determined by averaging signals of 1-Kb around the center of the indicated regions. *p* value was determined by Kolmogorov–Smirnov test.

(E) RNA fluorescence in situ hybridization (RNA-FISH) of the indicated tissue sections including diaphragm metastasis from KPC mice using a *Foxa1*-specific probe (red). Two independent KPC primary tumor and metastatic lesions were examined. White arrows indicate areas of focal *Foxa1* mRNA expression in primary PDA tumors. Counterstain, DAPI (blue). Scale bars, 100 μ m.

(F) Microarray-based FOXA1 mRNA expression in publicly available PDA patient data. Each dot represents individual patient. The mean \pm SEM is shown. *p* values were determined by Student's *t* test.

(G) FOXA1 expression during pancreatic differentiation of human embryonic stem cells (hES) relative to foregut stage.

(H) Gene set enrichment analysis (GSEA) of posterior foregut versus hES RNA-seq using a signature of *GAIN* genes. Normalized enrichment score (NES) and nominal *p* value (*p*) were provided according to GSEA.

(I) GSEA of averaged six M (M^{avg}) versus averaged six T (T^{avg}) RNA-seq using posterior foregut signature genes.

See also Figure S3 and Table S3.

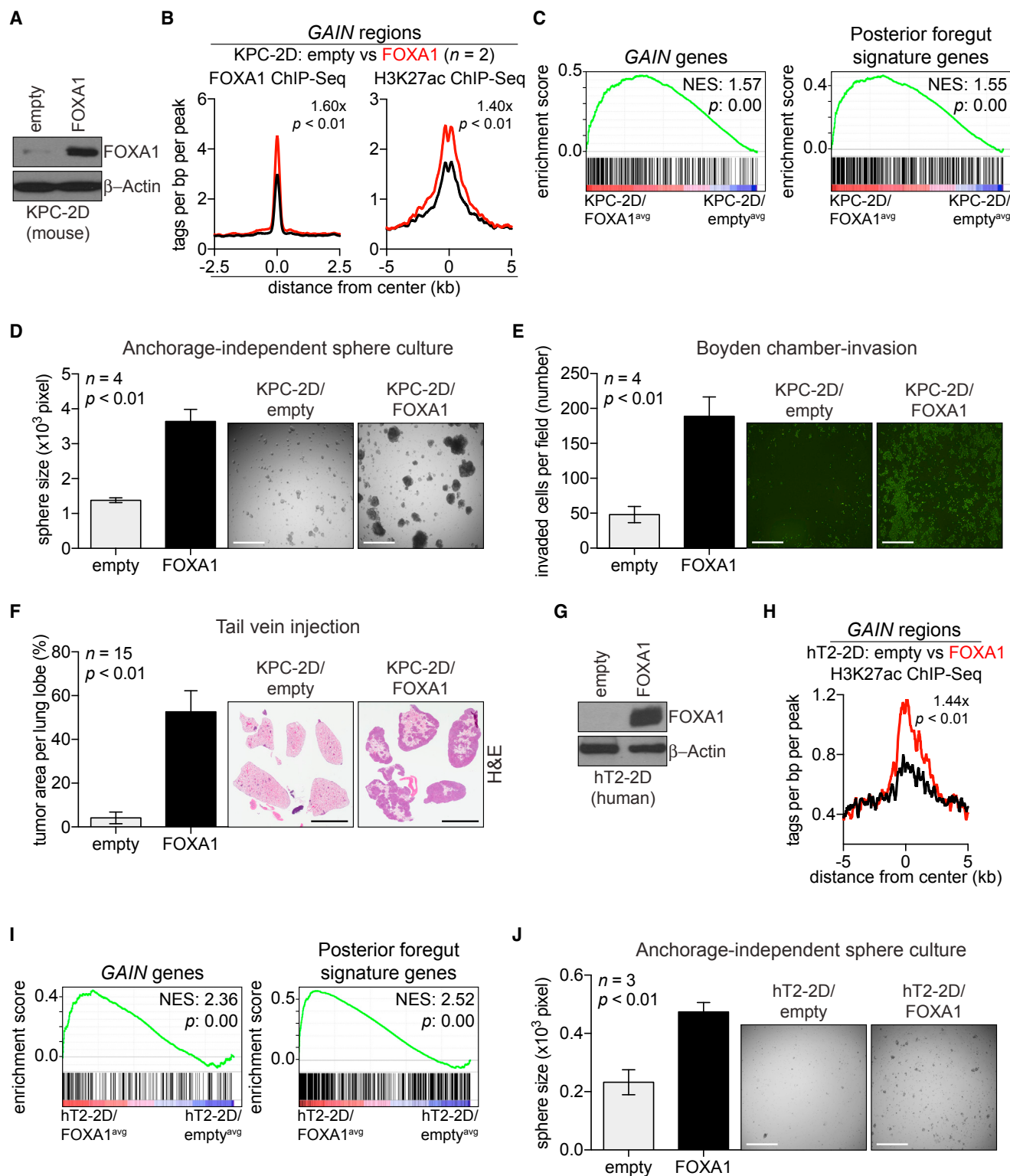


Figure 4. FOXA1 Promotes Enhancer activation and Metastatic Capabilities in 2D PDA Cell Lines

(A) Western blot analysis with the indicated antibodies and whole-cell lysates prepared from KPC-2D cells stably expressing FOXA1 cDNA (KPC-2D/FOXA1) or control (KPC-2D/empty).

(legend continued on next page)

We considered whether GATA5 cooperates with FOXA1 to promote *GAIN* enhancer activation in the organoid culture model. GATA5 expression alone had only a 1.1-fold effect on H3K27ac at *GAIN* regions in T organoids, but co-expression of GATA5 with FOXA1 led to a more robust activation of *GAIN* enhancers than expressing either TF alone, which recapitulated ~42% of the H3K27ac enrichment seen in M organoids (Figures 5B, 5C, and S5M). Overexpressing FOXA1 and GATA5 in T organoids also led to upregulation of *GAIN* genes and the foregut endoderm gene signature (Figure 5D). T organoids overexpressing FOXA1 and GATA5 or empty vector were injected into the pancreas of recipient mice, followed by evaluation of disease progression using ultrasound imaging. At a 12-week time-point, mice transplanted with FOXA1- and GATA5-expressing tumors required sacrifice due to their moribund condition, which was correlated with more rapid PDA tumor formation at the primary site than control mice (Figures 5E and 5F). Histological assessment of sacrificed animals revealed a higher frequency of metastasis in mice transplanted with FOXA1- and GATA5-expressing cells (Figures 5G and S5N–S5P). We also found that FOXA1 and GATA5 co-expressing T organoids developed larger tumors when injected subcutaneously, which resembles the aggressiveness of M organoids (Figures 1G and 5H). These findings show that GATA5 cooperates with FOXA1 to activate *GAIN* enhancers and promote PDA progression in vivo.

We next evaluated the necessity of FOXA1 to maintain the aggressive properties of M organoids by generating FOXA1-deficient M^{1L} organoids with short hairpin RNA-mediated knockdown or with CRISPR-Cas9 genome editing. shRNA-expressing cells had reduced FOXA1 occupancy in association with reduced H3K27ac at *GAIN* regions (Figures 6A–6C and S6A–S6C). RNA-seq analysis of FOXA1-deficient M organoids revealed downregulation of *GAIN* genes and the foregut endoderm gene signature (Figure 6D). This result prompted us to investigate PDA progression following transplantation of FOXA1-deficient

M^{1L} organoids into the pancreas of recipient mice. At 6 weeks post-transplant, FOXA1 knockdown led to significantly smaller primary tumors in the pancreas (average tumor weight of 10 mice, shRen; 0.91 g /shFoxa1 0.57 g, $p < 0.01$) (Figure 6E). In addition, we identified metastases in 4 out of 10 control mice, whereas Foxa1 knockdown was associated with metastasis in only 1 out of 10 mice (Figures 6F and S6D). Similar findings were observed using CRISPR-based targeting of *Foxa1* (Figures S6E–S6J). Taken together, these findings suggest that FOXA1-dependent enhancer reprogramming promotes PDA progression and metastasis in vivo.

DISCUSSION

The central conclusion of our study is that a reorganization of the enhancer landscape promotes metastasis in pancreatic cancer. The initial support for this conclusion comes from our epigenomic profiling of organoid cultures derived from each stage of PDA progression in the KPC mouse model, which revealed prominent gains and losses of enhancer activity associated with the metastatic transition. The recurrent pattern of enhancer activation among independent metastatic lesions suggests a functional role for these *cis* elements during metastatic progression. We identify FOXA1 upregulation as a key driver of this process, which can promote enhancer activation and metastasis in vivo. In this setting, FOXA1 activates an embryonic foregut endoderm transcriptional program, which, to our knowledge, is a process that has not been previously implicated as a source of metastatic traits.

During embryonic development, FOXA1 functions redundantly with FOXA2 to specify the definitive endoderm and to allow development of foregut-derived organs, which includes the pancreas (Gao et al., 2008). While FOXA2 expression is high in the normal adult pancreatic ductal epithelium, its expression decreases and becomes replaced by FOXA1 during

(B) Metagene representation of the mean FOXA1 (left) or H3K27ac (right) ChIP-seq signal across *GAIN* regions in the indicated organoids. The mean signal of each biological replicate was determined by averaging signals of 1-Kb (FOXA1) or 2-Kb (H3K27ac) around the center of the indicated regions. p value was determined by Kolmogorov–Smirnov test.

(C) GSEA of averaged KPC-2D/FOXA1 (FOXA1^{av9}) versus averaged KPC-2D/empty (empty^{av9}) RNA-seq using *GAIN* genes (left) and posterior foregut signature genes (right).

(D) Anchorage-independent sphere formation assay of KPC-2D/empty and KPC-2D/FOXA1 cells ($n = 4$). Bright field images were taken from 4× field after 2 weeks of culture, and the size of spheres were measured for quantification. The mean \pm SEM is shown, and p value was determined by Student's t test. Scale bars, 500 μ m.

(E) Boyden-chamber invasion assay of KPC-2D/empty and KPC-2D/FOXA1 cells ($n = 4$). Invaded cells were stained with Syto13 (GFP) 24 hr after cell seeding. Fluorescent microscopic images were taken from 4× field (right) to quantify the number of invaded cells (left). The mean \pm SEM is shown, and p value was determined by Student's t test. Scale bars, 500 μ m.

(F) Tail vein injection of KPC-2D/empty and KPC-2D/FOXA1 cells (2.5×10^5 cells) into C57BL/6J mice to assess lung colonization at 4 weeks post-injection. Representative images of H&E staining are shown (right). Percent tumor area per lung lobe (%) was determined by dividing the whole surface area of the largest lung lobe with lung tumor area of the given lobe. The mean \pm SEM is shown, and p value was determined by Student's t test ($n = 15$). Scale bars, 5 mm.

(G) Western blot analysis with the indicated antibodies and whole-cell lysates prepared from hT2-2D cells stably expressing FOXA1 cDNA (hT2-2D/FOXA1) or control (hT2-2D/empty).

(H) Metagene representation of H3K27ac ChIP-seq signal across *GAIN* regions in hT2-2D cells. The mean signal of each biological replicate was determined by averaging signals of 2-Kb H3K27ac around the center of the indicated regions. p value was determined by Kolmogorov–Smirnov test.

(I) GSEA of hT2-2D/FOXA1 versus hT2-2D/empty using a signature of *GAIN* genes (left) and posterior foregut signature genes (right). Normalized enrichment score (NES) and nominal p value (p) were provided according to GSEA.

(J) Anchorage-independent sphere formation assay of hT2-2D/empty and hT2-2D/FOXA1 cells ($n = 3$). Bright field images were taken from 4× field after 2 weeks of culture, and the size of spheres was measured for quantification. The mean \pm SEM is shown, and p value was determined by Student's t test. Scale bars, 500 μ m.

See also Figure S4 and Table S4 and S5.

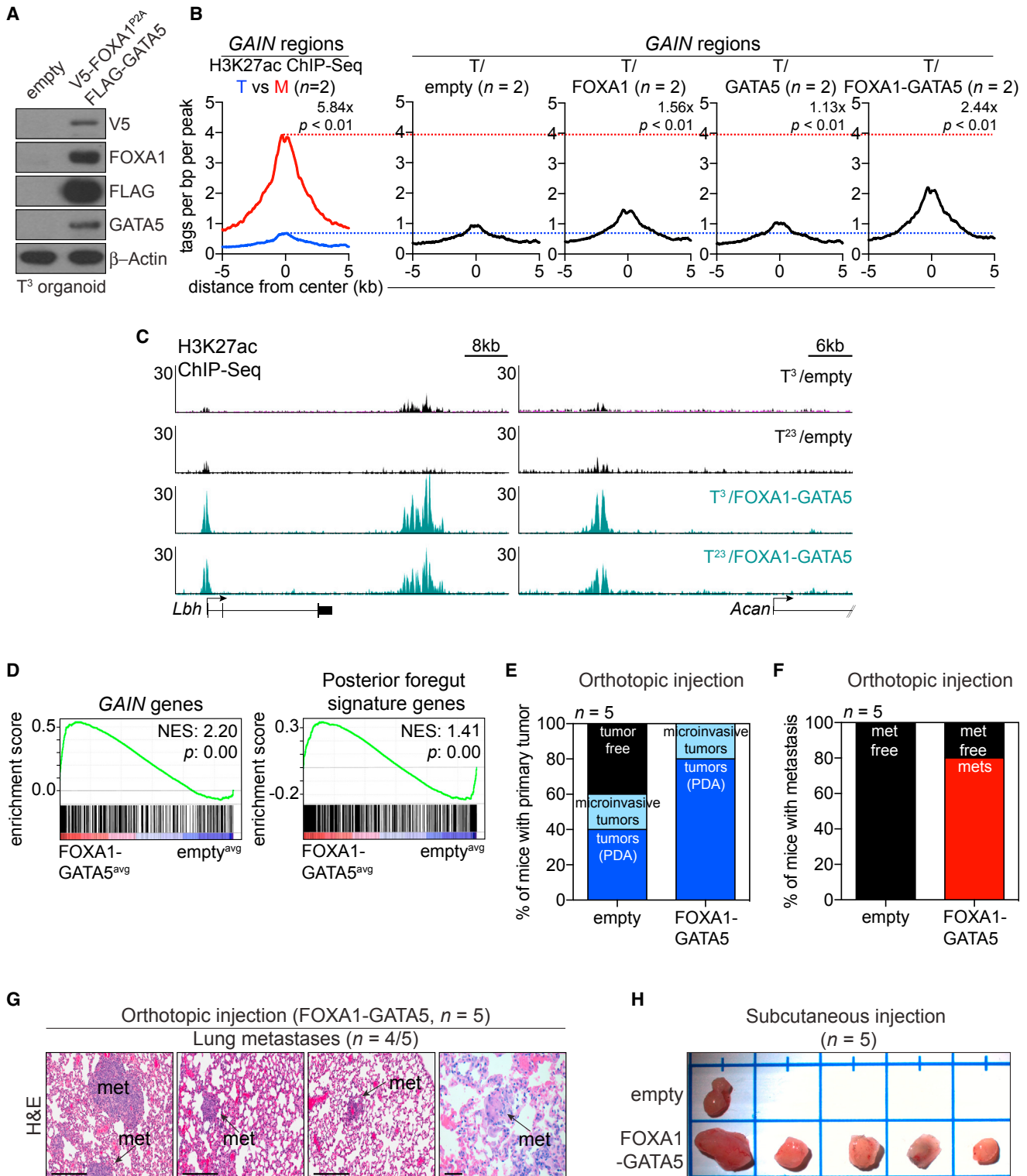


Figure 5. FOXA1 Cooperates with GATA5 to Activate GAIN Enhancers and Promote PDA Progression In Vivo

(A) Western blot analysis of T³/empty or T³/FOXA1-GATA5 organoids with the indicated antibodies. (B) Metagene representation of the mean H3K27ac ChIP-seq signal across GAIN regions in the indicated organoids. Mean H3K27ac signal of two parental T organoids (T³ and T²³) and their matched M organoids (M^{1L} and M^{1OP}) are displayed (left). T³ and T²³ organoids stably expressing control, FOXA1, GATA5, or FOXA1-GATA5 construct were subjected to H3K27ac ChIP-seq to compare with parental T (blue dotted line) or matched M (red dotted line) organoids.

(legend continued on next page)

PDA progression. Our transcriptional profiling experiments have suggested that the aberrant upregulation of FOXA1 in PDA leads to activation of foregut endoderm genes. This finding implies that genes expressed during this developmental transition can be repurposed to endow tumor cells with metastatic capabilities. We note that many of the foregut endoderm genes activated by FOXA1 in PDA metastasis encode signaling molecules that might allow for anchorage-independent growth or invasive properties, e.g., *RGL1* (Vigil et al., 2010). Foregut endoderm development is also a process of rapid cell proliferation and branching morphogenesis of epithelial cells that invade into mesenchymal tissues (Larsen and Grapin-Botton, 2017). Such cellular characteristics bear an obvious commonality with the characteristics of metastatic cancer cells and may explain the re-emergence of developmental programs during PDA progression.

A link between FOXA1 and PDA metastasis was unexpected, as prior studies have shown that FOXA1 is expressed at lower levels in mesenchymal (also referred to as “high-grade”) PDA cell lines (Bailey et al., 2016; Diaferia et al., 2016; Song et al., 2010). However, our analysis of murine and human PDA samples shows that FOXA1 upregulation is a prevalent feature among advanced primary tumors and metastatic lesions in this disease (Moffitt et al., 2015). This discrepancy can be accounted for by considering the recently identified subtypes of PDA revealed by transcriptome analysis (Bailey et al., 2016). FOXA1 upregulation is associated with a “progenitor” (also known as classical) subtype of PDA, whereas FOXA1 expression is low in the “squamous” (also known as quasi-mesenchymal) subtype (Bailey et al., 2016; Collisson et al., 2011). Both of these PDA subtypes are highly metastatic, with only small differences in overall patient survival (Bailey et al., 2016). This raises the possibility that these subtypes achieve their metastatic potential through distinct mechanisms, which may explain why high FOXA1 expression does not correlate with an exceptionally poor patient outcome (data not shown).

Our functional experiments demonstrate that FOXA1-mediated enhancer reprogramming increases metastatic potential, but also confers a fitness advantage to cells in the primary tumor. This observation is consistent with measurements of FOXA1 expression in mouse and human PDA samples, in which we observe progressive FOXA1 upregulation in primary tumors and metastasis. In the KPC model, we observe the

most striking FOXA1 upregulation in metastatic lesions, with only occasional regions of focal expression detected in primary tumors. In human PDA, FOXA1 becomes upregulated in primary tumors in a manner that correlates with disease stage, with additional FOXA1 upregulation in metastatic lesions (Moffitt et al., 2015). These species-specific differences are likely due to distinct clonal dynamics in the genetically engineered mouse model versus the spontaneous genetic events that drive the human disease. Nevertheless, a priority for future investigation will be to map enhancers at single-cell resolution in matched primary tumors and metastases from human PDA patients to gain a deeper understanding of how enhancer reprogramming participates in the clonal evolution of this heterogeneous disease.

TP53 mutations occur frequently during PDA progression, particularly in the late stage of PanINs (Hruban et al., 2000). Laser capture microdissection studies on PDA specimens have revealed that p53 loss-of-heterozygosity (LOH) occurs in focal areas of primary tumors and is frequently found in invasive lesions (Sakai et al., 2000; Yamano et al., 2000). Recurrent p53 LOH and FOXA1 upregulation in M organoids raised the possibility that FOXA1 upregulation might be caused by p53 LOH during metastasis. However, our data indicate that FOXA1-mediated enhancer reprogramming occurs independently of p53 LOH. Since p53 has been proposed to regulate epigenetic states (Levine and Greenbaum, 2012) and p53 LOH has been shown as an important driver of PDA progression (Muzumdar et al., 2016), it is still possible that tumor cells with p53 LOH become more permissive to epigenetic alterations in certain contexts, such as stromal cues or metabolic challenges. Nonetheless, this requires further investigation to determine whether cooperativity exists between enhancer reprogramming and p53 LOH in PDA progression and metastasis in vivo.

An emerging body of evidence implicates chromatin deregulation in the acquisition of metastatic traits. In a recent study, small-cell lung cancer metastasis was associated with widespread increases in chromatin accessibility across the genome, as a consequence of NFIB amplification (Denny et al., 2016). This mechanism appears to be distinct from our observations in PDA, since we did not observe generalized increases in chromatin accessibility associated with metastasis in this setting. Disruption of large heterochromatin domains of H3K9/H4K20 methylation has also recently been linked with PDA metastasis

Parental T organoids were compared with matched M organoids, and T/FOXA1 or T/FOXA1-GATA5 organoids were compared with T/empty organoids. The mean signal of each biological replicate was determined by averaging signals of 2-Kb around the center of the indicated regions. *p* value was determined by Kolmogorov-Smirnov test.

(C) Representative H3K27ac ChIP-seq profiles of *GAIN* regions at *Lbh* and *Acan* loci in the indicated organoids.

(D) GSEA of averaged T/FOXA1-GATA5 (FOXA1-GATA5^{av9}) versus averaged T/empty (empty^{av9}) RNA-seq using *GAIN* genes (left) or posterior foregut signature genes (right).

(E and F) Quantification of the number of mice with primary tumors at injection site (pancreas, E) and metastases (F) after orthotopic injection of T³/empty or T³/FOXA1-GATA5 organoids in athymic nu/nu mice (*n* = 5). 5 × 10⁵ cells were orthotopically injected and mice were sacrificed at 12 weeks post-injection. Frequency of PDA and microinvasive PDA development in orthotopic injection is 40% (*n* = 2/5) and 20% (*n* = 1/5), respectively, for T³/empty and 80% (*n* = 4/5) and 20% (*n* = 1/5), respectively, for T³/FOXA1-GATA5.

(G) H&E staining of lung micrometastases (*n* = 4/5, arrows) upon orthotopic injection of T³/FOXA1-GATA5 organoids. Scale bars, 200 μm.

(H) Tumor development after subcutaneous injection of T³/empty and T³/FOXA1-GATA5 organoids. 5 × 10⁵ of cells were subcutaneously injected into C57BL/6J mice and mice were sacrificed at 11 weeks post-injection. Note, four of T³/empty-injected mice (*n* = 5) did not show apparent subcutaneous tumor formation in a syngeneic background.

See also Figure S5 and Tables S4 and S5.

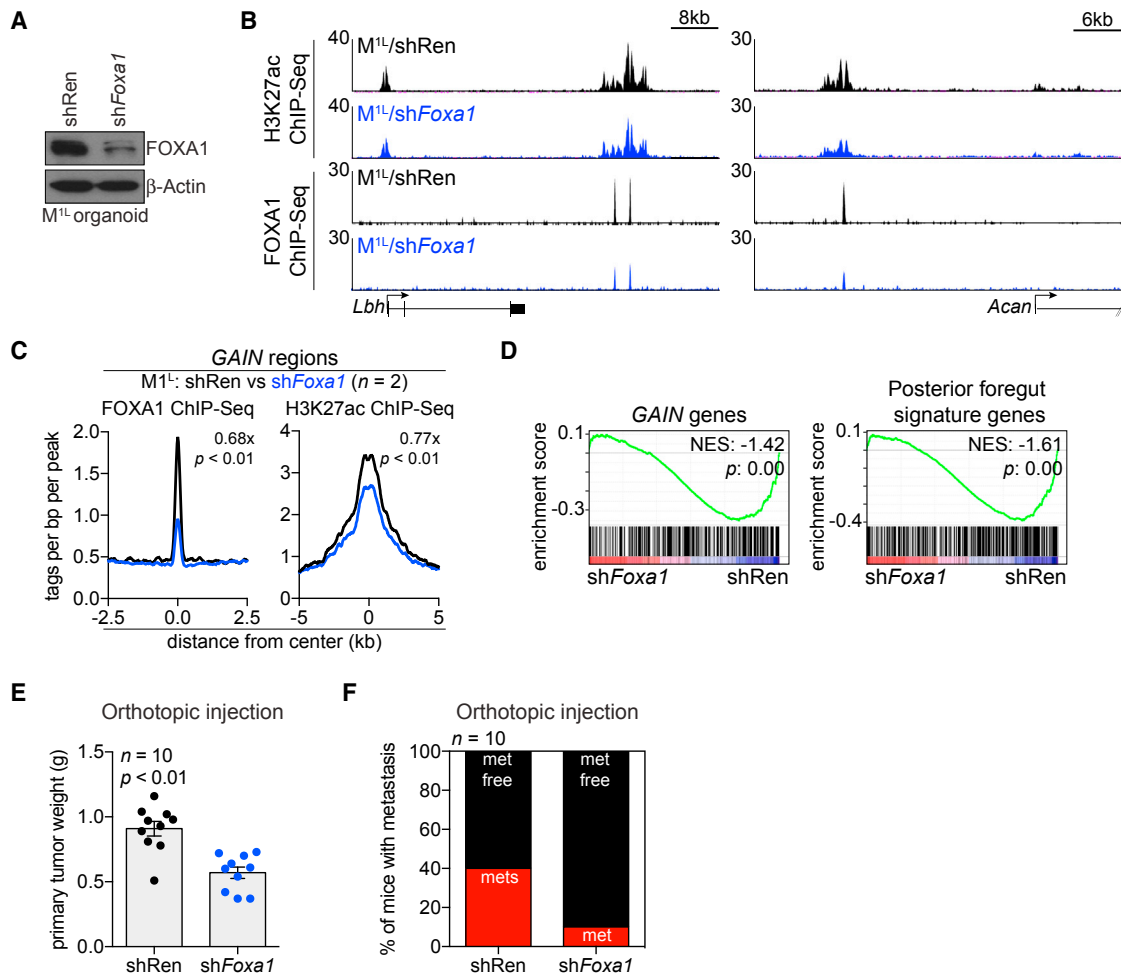


Figure 6. Suppression of FOXA1 Deactivates GAIN Enhancers and Diminishes the Aggressiveness of Metastasis-Derived PDA Organoids

(A) Western blotting of M^{1L} organoids stably expressing shRen (M^{1L}/shRen) or shFoxa1.2959 construct (M^{1L}/shFoxa1) with the indicated antibodies.
 (B) Representative H3K27ac ChIP-seq profiles of GAIN regions at *Lbh* and *Acan* loci in the indicated organoids.
 (C) Metagene representation of the mean FOXA1 (left) or H3K27ac (right) ChIP-seq signal across GAIN regions in the indicated organoids. The mean signal of each biological replicate was determined by averaging signals of 1-Kb (FOXA1) or 2-Kb (H3K27ac) around the center of the indicated regions. *p* value was determined by Kolmogorov-Smirnov test.
 (D) GSEA of M^{1L}/shFoxa1 versus M^{1L}/shRen using GAIN genes (left) or posterior foregut signature genes (right).
 (E) Quantification of primary tumor weight from injection site (pancreas) after orthotopic injection of M/shRen or M/shFoxa1 organoids in athymic nu/nu mice (*n* = 10). 5 × 10⁵ cells were orthotopically injected and mice were sacrificed at 6 weeks post-injection. Each dot represents a mouse, and the mean ± SEM is shown. *p* value was determined by Student's *t* test.
 (F) Quantification of the number of mice bearing metastasis upon orthotopic injection of M/shRen or M/shFoxa1 organoids (*n* = 10).
 See also [Figure S6](#) and [Tables S4](#) and [S5](#).

(McDonald et al., 2017). Within this larger body of evidence of epigenetic deregulation in metastasis, our study calls attention to alterations of the enhancer landscape as a mechanism by which tumor cells gain metastatic potential. These findings raise the possibility that targeting enhancer-binding proteins, such as the writers, readers, and erasers of chromatin marks, will provide a means of eliminating metastatic disease.

STAR★METHODS

Detailed methods are provided in the online version of this paper and include the following:

- [KEY RESOURCES TABLE](#)
- [CONTACT FOR REAGENT AND RESOURCE SHARING](#)
- [EXPERIMENTAL MODEL AND SUBJECT DETAILS](#)
 - Mice
 - Organoids, cell lines and culture conditions
 - Human specimens
- [METHOD DETAILS](#)
 - Next-generation sequencing library constructions
 - Protein and DNA/RNA-related experiments
 - Cell culture-related experiments
 - In vivo experiments
 - Computational analyses

- QUANTIFICATION AND STATISTICAL ANALYSIS
- DATE AND SOFTWARE AVAILABILITY

SUPPLEMENTAL INFORMATION

Supplemental Information includes six figures and six tables and can be found with this article online at <http://dx.doi.org/10.1016/j.cell.2017.07.007>.

AUTHOR CONTRIBUTIONS

J.-S.R., C.-I.H., D.A.T., and C.R.V. conceptualized this study and designed the experiments. J.-S.R. and C.-I.H. performed the majority of the experiments and contributed equally to this work. C.-I.H., E.J.L., B.D.S., D.F., B.C., and Y.P. established and characterized murine PDA organoids used in this study. J.-S.R. and C.-I.H. conducted ChIP-seq, ATAC-seq, and RNA-seq experiments. J.-S.R. conducted the majority of bioinformatics analysis. C.-I.H. conducted the majority of in vivo experiments. C.-I.H. and D.A.T. interpreted in vivo experiments. J.-S.R. conducted and interpreted in vitro metastasis assay experiments. J.-S.R., C.-I.H., and J.P.M. conducted and interpreted tail vein injection experiments. T.D.D.S. profiled gene expression in human organoid samples and performed in vitro assays with human cell lines. H.T., C.M.Y., K.M., and R.A.B. optimized human organoid methods and isolated patient-derived organoids. R.A.B., J.M.B., and E.J.K. provided clinical specimens. L.M. and M.E. performed portal vein injection experiments and assisted in vitro and in vivo metastasis experiments. P.M.G., M.A.H., J.L.G., A.J.L., and J.A.G. were involved in rapid autopsy program for human specimens. J.-S.R., C.-I.H., D.A.T., and C.R.V. wrote this manuscript. D.A.T. and C.R.V. supervised throughout the study.

ACKNOWLEDGMENTS

We would like to thank all members of the C.R.V. and D.A.T. laboratories for helpful discussions and suggestions throughout the course of this study. The authors would like to thank the Cold Spring Harbor Cancer Center Support Grant (CCSG, P30CA045508-29) shared resources: Bioinformatics Shared Resource, Microscope, DNA Sequencing, Animal & Tissue Imaging, and the Animal Facility. We are grateful to Junichi Takagi at Osaka University for sharing the Afamin/Wnt3A cell line. This project was also funded by NCI 5P01CA013106-Project 4 (C.R.V.), a Career Development Award from the Pancreatic Cancer Action Network-AACR 16-20-25-VAKO (C.R.V.), and the Lustgarten Foundation, where D.A.T. is a distinguished scholar and Director of the Lustgarten Foundation-designated Laboratory of Pancreatic Cancer Research. D.A.T. is also supported by the Cold Spring Harbor Laboratory Association, the National Institutes of Health (NIH; 5P30CA45508-29, 5P50CA101955-07, 1U10CA180944-04, 5U01CA168409-5, 1R01CA188134-01, and 1R01CA190092-04), and the V Foundation. In addition, we are grateful for support from the following: Stand Up to Cancer/AACR PS09 (D.A.T.), NCI (1F32CA180717-01A1 for C.-I.H. and P50CA127297 for P.M.G., M.A.H., J.L.G., A.J.L., and J.A.G.), Daiichi Sankyo Foundation of Life Science fellowship and Uehara Memorial Foundation research fellowship (K.M.), Stony Brook pilot project grant (J.M.B.), ASGE (J.M.B.), SWOG ITSC 5U10CA180944-04 (E.J.K., D.A.T., H.T.), and NIH (R50CA211506-01 for Y.P., P20CA19299402 for J.M.B. and D.A.T., and 5T32CA126607-08 for R.A.B.).

Received: April 13, 2017

Revised: May 29, 2017

Accepted: July 7, 2017

Published: July 27, 2017

REFERENCES

Abraham, B.J., Hnisz, D., Weintraub, A.S., Kwiatkowski, N., Li, C.H., Li, Z., Weichert-Leahey, N., Rahman, S., Liu, Y., Etchin, J., et al. (2017). Small genomic insertions form enhancers that misregulate oncogenes. *Nat. Commun.* **8**, 14385.

Arda, H.E., Li, L., Tsai, J., Torre, E.A., Rosli, Y., Peiris, H., Spitale, R.C., Dai, C., Gu, X., Qu, K., et al. (2016). Age-dependent pancreatic gene regulation reveals mechanisms governing human beta cell function. *Cell Metab.* **23**, 909–920.

Bailey, P., Chang, D.K., Nones, K., Johns, A.L., Patch, A.M., Gingras, M.C., Miller, D.K., Christ, A.N., Bruxner, T.J., Quinn, M.C., et al.; Australian Pancreatic Cancer Genome Initiative (2016). Genomic analyses identify molecular subtypes of pancreatic cancer. *Nature* **531**, 47–52.

Boj, S.F., Hwang, C.I., Baker, L.A., Chio, I.I., Engle, D.D., Corbo, V., Jager, M., Ponz-Sarvisse, M., Tiriari, H., Spector, M.S., et al. (2015). Organoid models of human and mouse ductal pancreatic cancer. *Cell* **160**, 324–338.

Buenrostro, J.D., Giresi, P.G., Zaba, L.C., Chang, H.Y., and Greenleaf, W.J. (2013). Transposition of native chromatin for fast and sensitive epigenomic profiling of open chromatin, DNA-binding proteins and nucleosome position. *Nat. Methods* **10**, 1213–1218.

Campbell, P.J., Yachida, S., Mudie, L.J., Stephens, P.J., Pleasance, E.D., Stebbings, L.A., Morsberger, L.A., Latimer, C., McLaren, S., Lin, M.L., et al. (2010). The patterns and dynamics of genomic instability in metastatic pancreatic cancer. *Nature* **467**, 1109–1113.

Chio, I.I., Jafarnejad, S.M., Ponz-Sarvisse, M., Park, Y., Rivera, K., Palm, W., Wilson, J., Sangar, V., Hao, Y., Öhlund, D., et al. (2016). NRF2 Promotes Tumor Maintenance by Modulating mRNA Translation in Pancreatic Cancer. *Cell* **166**, 963–976.

Christensen, C.L., Kwiatkowski, N., Abraham, B.J., Carretero, J., Al-Shahrour, F., Zhang, T., Chipumuro, E., Herter-Sprie, G.S., Akbay, E.A., Altabel, A., et al. (2014). Targeting transcriptional addictions in small cell lung cancer with a covalent CDK7 inhibitor. *Cancer Cell* **26**, 909–922.

Collisson, E.A., Sadanandam, A., Olson, P., Gibb, W.J., Truitt, M., Gu, S., Cooc, J., Weinkle, J., Kim, G.E., Jakkula, L., et al. (2011). Subtypes of pancreatic ductal adenocarcinoma and their differing responses to therapy. *Nat. Med.* **17**, 500–503.

Denny, S.K., Yang, D., Chuang, C.H., Brady, J.J., Lim, J.S., Grüner, B.M., Chiou, S.H., Schep, A.N., Baral, J., Hamard, C., et al. (2016). Nf1b Promotes Metastasis through a Widespread Increase in Chromatin Accessibility. *Cell* **166**, 328–342.

Diaferia, G.R., Balestrieri, C., Prosperini, E., Nicoli, P., Spaggiari, P., Zerbi, A., and Natoli, G. (2016). Dissection of transcriptional and cis-regulatory control of differentiation in human pancreatic cancer. *EMBO J.* **35**, 595–617.

Fellmann, C., Hoffmann, T., Sridhar, V., Hopfgartner, B., Muhar, M., Roth, M., Lai, D.Y., Barbosa, I.A., Kwon, J.S., Guan, Y., et al. (2013). An optimized micro-RNA backbone for effective single-copy RNAi. *Cell Rep.* **5**, 1704–1713.

Gao, N., LeLay, J., Vatamaniuk, M.Z., Rieck, S., Friedman, J.R., and Kaestner, K.H. (2008). Dynamic regulation of Pdx1 enhancers by Foxa1 and Foxa2 is essential for pancreas development. *Genes Dev.* **22**, 3435–3448.

Guerra, C., and Barbacid, M. (2013). Genetically engineered mouse models of pancreatic adenocarcinoma. *Mol. Oncol.* **7**, 232–247.

Heinz, S., Benner, C., Spann, N., Bertolino, E., Lin, Y.C., Laslo, P., Cheng, J.X., Murre, C., Singh, H., and Glass, C.K. (2010). Simple combinations of lineage-determining transcription factors prime cis-regulatory elements required for macrophage and B cell identities. *Mol. Cell* **38**, 576–589.

Hessmann, E., Johnsen, S.A., Siveke, J.T., and Ellenrieder, V. (2017). Epigenetic treatment of pancreatic cancer: is there a therapeutic perspective on the horizon? *Gut* **66**, 168–179.

Hingorani, S.R., Wang, L., Multani, A.S., Combs, C., Deramandt, T.B., Hruban, R.H., Rustgi, A.K., Chang, S., and Tuveson, D.A. (2005). Trp53R172H and KrasG12D cooperate to promote chromosomal instability and widely metastatic pancreatic ductal adenocarcinoma in mice. *Cancer Cell* **7**, 469–483.

Hruban, R.H., Goggins, M., Parsons, J., and Kern, S.E. (2000). Progression model for pancreatic cancer. *Clin. Cancer Res.* **6**, 2969–2972.

Kong, S.L., Li, G., Loh, S.L., Sung, W.K., and Liu, E.T. (2011). Cellular reprogramming by the conjoint action of ER α , FOXA1, and GATA3 to a ligand-inducible growth state. *Mol. Syst. Biol.* **7**, 526.

- Krebs, A.M., Mitschke, J., Lasierra Losada, M., Schmalhofer, O., Boerries, M., Busch, H., Boettcher, M., Mougiakakos, D., Reichardt, W., Bronsert, P., et al. (2017). The EMT-activator Zeb1 is a key factor for cell plasticity and promotes metastasis in pancreatic cancer. *Nat. Cell Biol.* **19**, 518–529.
- Kugel, S., Sebastián, C., Fitamant, J., Ross, K.N., Saha, S.K., Jain, E., Gladden, A., Arora, K.S., Kato, Y., Rivera, M.N., et al. (2016). SIRT6 Suppresses Pancreatic Cancer through Control of Lin28b. *Cell* **165**, 1401–1415.
- Langmead, B., Trapnell, C., Pop, M., and Salzberg, S.L. (2009). Ultrafast and memory-efficient alignment of short DNA sequences to the human genome. *Genome Biol.* **10**, R25.
- Larsen, H.L., and Grapin-Botton, A. (2017). The molecular and morphogenetic basis of pancreas organogenesis. *Semin. Cell Dev. Biol.* **66**, 51–68.
- Levine, A.J., and Greenbaum, B. (2012). The maintenance of epigenetic states by p53: the guardian of the epigenome. *Oncotarget* **3**, 1503–1504.
- Li, H., Handsaker, B., Wysoker, A., Fennell, T., Ruan, J., Homer, N., Marth, G., Abecasis, G., and Durbin, R.; 1000 Genome Project Data Processing Subgroup (2009). The Sequence Alignment/Map format and SAMtools. *Bioinformatics* **25**, 2078–2079.
- Lin, C.Y., Lovén, J., Rahl, P.B., Paranal, R.M., Burge, C.B., Bradner, J.E., Lee, T.I., and Young, R.A. (2012). Transcriptional amplification in tumor cells with elevated c-Myc. *Cell* **151**, 56–67.
- Loh, K.M., Ang, L.T., Zhang, J., Kumar, V., Ang, J., Auyeong, J.Q., Lee, K.L., Choo, S.H., Lim, C.Y., Nichane, M., et al. (2014). Efficient endoderm induction from human pluripotent stem cells by logically directing signals controlling lineage bifurcations. *Cell Stem Cell* **14**, 237–252.
- Long, H.K., Prescott, S.L., and Wysocka, J. (2016). Ever-Changing Landscapes: Transcriptional Enhancers in Development and Evolution. *Cell* **167**, 1170–1187.
- Makohon-Moore, A.P., Zhang, M., Reiter, J.G., Bozic, I., Allen, B., Kundu, D., Chatterjee, K., Wong, F., Jiao, Y., Kohutek, Z.A., et al. (2017). Limited heterogeneity of known driver gene mutations among the metastases of individual patients with pancreatic cancer. *Nat. Genet.* **49**, 358–366.
- McDonald, O.G., Li, X., Saunders, T., Tryggvadottir, R., Mentch, S.J., Warms, M.O., Word, A.E., Carrer, A., Salz, T.H., Natsume, S., et al. (2017). Epigenomic reprogramming during pancreatic cancer progression links anabolic glucose metabolism to distant metastasis. *Nat. Genet.* **49**, 367–376.
- McLean, C.Y., Bristol, D., Hiller, M., Clarke, S.L., Schaar, B.T., Lowe, C.B., Wenger, A.M., and Bejerano, G. (2010). GREAT improves functional interpretation of cis-regulatory regions. *Nat. Biotechnol.* **28**, 495–501.
- Mihara, E., Hirai, H., Yamamoto, H., Tamura-Kawakami, K., Matano, M., Kikuchi, A., Sato, T., and Takagi, J. (2016). Active and water-soluble form of lipidated Wnt protein is maintained by a serum glycoprotein afamin/ α -albumin. *eLife* **5**, e11621.
- Moffitt, R.A., Marayati, R., Flate, E.L., Volmar, K.E., Loeza, S.G., Hoadley, K.A., Rashid, N.U., Williams, L.A., Eaton, S.C., Chung, A.H., et al. (2015). Virtual microdissection identifies distinct tumor- and stroma-specific subtypes of pancreatic ductal adenocarcinoma. *Nat. Genet.* **47**, 1168–1178.
- Muzumdar, M.D., Dorans, K.J., Chung, K.M., Robbins, R., Tammela, T., Gocheva, V., Li, C.M., and Jacks, T. (2016). Clonal dynamics following p53 loss of heterozygosity in Kras-driven cancers. *Nat. Commun.* **7**, 12685.
- Neureiter, D., Jäger, T., Ocker, M., and Kiesslich, T. (2014). Epigenetics and pancreatic cancer: pathophysiology and novel treatment aspects. *World J. Gastroenterol.* **20**, 7830–7848.
- Öhlund, D., Elyada, E., and Tuveson, D. (2014). Fibroblast heterogeneity in the cancer wound. *J. Exp. Med.* **211**, 1503–1523.
- Olive, K.P., Tuveson, D.A., Ruhe, Z.C., Yin, B., Willis, N.A., Bronson, R.T., Crowley, D., and Jacks, T. (2004). Mutant p53 gain of function in two mouse models of Li-Fraumeni syndrome. *Cell* **119**, 847–860.
- Quinlan, A.R., and Hall, I.M. (2010). BEDTools: a flexible suite of utilities for comparing genomic features. *Bioinformatics* **26**, 841–842.
- Ryan, D.P., Hong, T.S., and Bardeesy, N. (2014). Pancreatic adenocarcinoma. *N. Engl. J. Med.* **371**, 1039–1049.
- Sakai, Y., Yanagisawa, A., Shimada, M., Hidaka, E., Seki, M., Tada, Y., Harada, T., Saisho, H., and Kato, Y. (2000). K-ras gene mutations and loss of heterozygosity at the p53 gene locus relative to histological characteristics of mucin-producing tumors of the pancreas. *Hum. Pathol.* **31**, 795–803.
- Sekiya, S., and Suzuki, A. (2011). Direct conversion of mouse fibroblasts to hepatocyte-like cells by defined factors. *Nature* **475**, 390–393.
- Shi, J., Wang, E., Milazzo, J.P., Wang, Z., Kinney, J.B., and Vakoc, C.R. (2015). Discovery of cancer drug targets by CRISPR-Cas9 screening of protein domains. *Nat. Biotechnol.* **33**, 661–667.
- Siegel, R.L., Miller, K.D., and Jemal, A. (2017). Cancer Statistics, 2017. *CA Cancer J. Clin.* **67**, 7–30.
- Soares, K.C., Foley, K., Olino, K., Leubner, A., Mayo, S.C., Jain, A., Jaffee, E., Schulick, R.D., Yoshimura, K., Edil, B., and Zheng, L. (2014). A preclinical murine model of hepatic metastases. *J. Vis. Exp.* **91**, 51677.
- Song, Y., Washington, M.K., and Crawford, H.C. (2010). Loss of FOXA1/2 is essential for the epithelial-to-mesenchymal transition in pancreatic cancer. *Cancer Res.* **70**, 2115–2125.
- Spitz, F., and Furlong, E.E. (2012). Transcription factors: from enhancer binding to developmental control. *Nat. Rev. Genet.* **13**, 613–626.
- Stelnicki, E.J., Arbeit, J., Cass, D.L., Saner, C., Harrison, M., and Largman, C. (1998). Modulation of the human homeobox genes PRX-2 and HOXB13 in scarless fetal wounds. *J. Invest. Dermatol.* **111**, 57–63.
- Thomas-Chollier, M., Hufton, A., Heinig, M., O’Keeffe, S., Masri, N.E., Roeder, H.G., Manke, T., and Vingron, M. (2011). Transcription factor binding predictions using TRAP for the analysis of ChIP-seq data and regulatory SNPs. *Nat. Protoc.* **6**, 1860–1869.
- Trapnell, C., Pachter, L., and Salzberg, S.L. (2009). TopHat: discovering splice junctions with RNA-Seq. *Bioinformatics* **25**, 1105–1111.
- Trapnell, C., Williams, B.A., Pertea, G., Mortazavi, A., Kwan, G., van Baren, M.J., Salzberg, S.L., Wold, B.J., and Pachter, L. (2010). Transcript assembly and quantification by RNA-Seq reveals unannotated transcripts and isoform switching during cell differentiation. *Nat. Biotechnol.* **28**, 511–515.
- Tripathi, S., Pohl, M.O., Zhou, Y., Rodriguez-Frandsen, A., Wang, G., Stein, D.A., Moulton, H.M., DeJesus, P., Che, J., Mulder, L.C., et al. (2015). Meta- and Orthogonal Integration of Influenza “OMICs” Data Defines a Role for UBR4 in Virus Budding. *Cell Host Microbe* **18**, 723–735.
- Vigil, D., Martin, T.D., Williams, F., Yeh, J.J., Campbell, S.L., and Der, C.J. (2010). Aberrant overexpression of the Rgl2 Ral small GTPase-specific guanine nucleotide exchange factor promotes pancreatic cancer growth through Ral-dependent and Ral-independent mechanisms. *J. Biol. Chem.* **285**, 34729–34740.
- Waddell, N., Pajic, M., Patch, A.M., Chang, D.K., Kassahn, K.S., Bailey, P., Johns, A.L., Miller, D., Nones, K., Quek, K., et al.; Australian Pancreatic Cancer Genome Initiative (2015). Whole genomes redefine the mutational landscape of pancreatic cancer. *Nature* **518**, 495–501.
- Weissmueller, S., Machado, E., Saborowski, M., Morris, J.P., 4th, Wagenblast, E., Davis, C.A., Moon, S.H., Pfister, N.T., Tschaharganeh, D.F., Kitzing, T., et al. (2014). Mutant p53 drives pancreatic cancer metastasis through cell-autonomous PDGF receptor β signaling. *Cell* **157**, 382–394.
- Whittle, M.C., Izeradjene, K., Rani, P.G., Feng, L., Carlson, M.A., DelGiorno, K.E., Wood, L.D., Goggins, M., Hruban, R.H., Chang, A.E., et al. (2015). RUNX3 Controls a Metastatic Switch in Pancreatic Ductal Adenocarcinoma. *Cell* **161**, 1345–1360.
- Xie, R., Everett, L.J., Lim, H.W., Patel, N.A., Schug, J., Kroon, E., Kelly, O.G., Wang, A., D’Amour, K.A., Robins, A.J., et al. (2013). Dynamic chromatin remodeling mediated by polycomb proteins orchestrates pancreatic differentiation of human embryonic stem cells. *Cell Stem Cell* **12**, 224–237.
- Yachida, S., Jones, S., Bozic, I., Antal, T., Leary, R., Fu, B., Kamiyama, M., Hruban, R.H., Eshleman, J.R., Nowak, M.A., et al. (2010). Distant metastasis occurs late during the genetic evolution of pancreatic cancer. *Nature* **467**, 1114–1117.

- Yamano, M., Fujii, H., Takagaki, T., Kadowaki, N., Watanabe, H., and Shirai, T. (2000). Genetic progression and divergence in pancreatic carcinoma. *Am. J. Pathol.* 156, 2123–2133.
- Ye, X., and Weinberg, R.A. (2015). Epithelial-Mesenchymal Plasticity: A Central Regulator of Cancer Progression. *Trends Cell Biol.* 25, 675–686.
- Yue, F., Cheng, Y., Breschi, A., Vierstra, J., Wu, W., Ryba, T., Sandstrom, R., Ma, Z., Davis, C., Pope, B.D., et al.; Mouse ENCODE Consortium (2014). A comparative encyclopedia of DNA elements in the mouse genome. *Nature* 515, 355–364.
- Zaret, K.S., Lerner, J., and Iwafuchi-Doi, M. (2016). Chromatin Scanning by Dynamic Binding of Pioneer Factors. *Mol. Cell* 62, 665–667.
- Zentner, G.E., and Scacheri, P.C. (2012). The chromatin fingerprint of gene enhancer elements. *J. Biol. Chem.* 287, 30888–30896.

STAR★METHODS

KEY RESOURCES TABLE

REAGENT or RESOURCE	SOURCE	IDENTIFIER
Antibodies		
Rabbit polyclonal anti-Foxa1 (for ChIP-Seq and WB)	Abcam	Ab23738; RRID: AB_2104842
Goat polyclonal anti-Foxa1 (for IHC)	Thermo Fisher	PA5-18168; RRID: AB_10986712
Rabbit polyclonal anti-Gata5 (for WB)	Abcam	Ab48820; RRID: AB_2108756
Rabbit polyclonal anti-H3K27ac (for ChIP-Seq)	Abcam	Ab4729; RRID: AB_2118291
Rabbit polyclonal anti-H3K4me1 (for ChIP-Seq)	Abcam	Ab8895; RRID: AB_306847
Rabbit polyclonal anti-H3 (for WB)	Abcam	Ab1791; RRID: AB_302613
Mouse monoclonal anti-Flag (for WB)	Sigma-Aldrich	F1804; RRID: AB_262044
Rabbit polyclonal anti-V5 (for WB)	Abcam	Ab9116; RRID: AB_307024
Rabbit polyclonal anti-Vinculin (for WB)	Cell Signaling	#4560; RRID: N/A
Mouse monoclonal anti- β -Actin-peroxidase (for WB)	Sigma-Aldrich	A3854; RRID: AB_262011
Rabbit polyclonal anti-p53 (for WB)	Santa Cruz biotechnology	SC-6243; RRID: AB_653753
Mouse monoclonal anti-p21 (for WB)	Santa Cruz biotechnology	SC-6246; RRID: AB_628073
ECL Rabbit IgG, HRP-linked whole Ab from donkey (for WB)	GE healthcare	NA394; RRID: N/A
Polyclonal rabbit anti-mouse immunoglobulins/HRP (for WB)	Agilent	P026002-2; RRID: AB_2636929
IgG from rabbit serum (for ChIP-Seq)	Sigma-Aldrich	I8140; RRID: AB_1163661
ImmPRESS HRP anti-goat IgG (peroxidase) polymer Detection kit (for IHC)	Vector Laboratories	MP-7405; RRID: AB_2336526
Biological Samples		
Human normal pancreas	University of Illinois at Chicago and University of Miami Miller School of Medicine. Boj et al., 2015 .	N/A
Human primary tumor and metastasis samples (from Rapid Autopsy Program)	University of Nebraska	N/A
Chemicals, Peptides and Recombinant Proteins		
Formaldehyde, 37% solution	Avantor	2106-01
Glycine	Fisher Scientific	BP381-1
Protease inhibitor cocktail	Sigma-Aldrich	11697498001
Dynabeads Protein A	Thermo Fisher	10002D
Ribonuclease A from bovine pancreas	Sigma-Aldrich	R4875
Proteinase K	New England Biolabs	P8107S
Agencourt AMPure XP	Beckman Coulter	A63880
SeaKem LE Agarose	Lonza	50004
TRIzol Reagent	Thermo Fisher	15596018
Chloroform	Sigma-Aldrich	288306
2-Propanol (Isopropanol)	Sigma-Aldrich	190674
DNase I (RNase-free)	New England Biolabs	M0303S
Q-Script cDNA SuperMix	Quanta bio	95048-500
Power SYBR Green Master Mix	Thermo Fisher	4368577
SuperScript II Reverse Transcriptase	Thermo Fisher	18064014
Crystal Violet	Sigma-Aldrich	C3886
Geneticin Selective Antibiotic (G418 Sulfate)	Thermo Fisher	10131035

(Continued on next page)

Continued

REAGENT or RESOURCE	SOURCE	IDENTIFIER
Puromycin dihydrochloride	Sigma-Aldrich	P8833
Polyethylenimine, Linear, MW 25,000 (PEI 25000)	Polysciences	23966-1
Hexadimethrine bromide (polybrene)	Sigma-Aldrich	H9268
2x Laemmli Sample Buffer	BIO-RAD	1610737
2-Mercaptoethanol	Sigma-Aldrich	M6250
30% Acrylamide/Bis Solution, 37.5:1	BIO-RAD	1610158
SuperSignal West Femto Maximum Sensitivity Substrate	Thermo Fisher	34095
SYTO13 Green Fluorescent Nucleic Acid Stain	Thermo Fisher	S7575
ImmPACT DAB peroxidase (HRP) substrate	Vector Laboratories	SK-4105
Collagenase Crude, Type XI (Clostridium histolyticum)	Sigma-Aldrich	C9407-1G
Dispase II	Life Technologies	17105041
DMEM with 4.5 g/L glucose, L-glutamine & sodium pyruvate	Cellgro	10-013-CV
Advanced DMEM/F12	Life Technologies	12634-028
RPMI 1640 w/ L-glutamine	Fisher Scientific	MT10040CV
HEPES	Life Technologies	15630-130
Glutamax	Life Technologies	35050-079
A83-01	Tocris Bioscience	2939
mEGF	Life Technologies	PMG8043
hEGF	PeprTech	AF-100-15
mNoggin	PeprTech	250-38
hFGF10	PeprTech	100-26
Gastrin I	Tocris Bioscience	3006
N-acetylcysteine	Sigma-Aldrich	A9165-5G
PGE2	Tocris Bioscience	2296
Nicotinamide	Sigma-Aldrich	N0636-100G
B-27 supplement	Life Technologies	17504044
R-Spondin1 Cells	Trevigen	3710-001-K
Afamin/Wnt3A conditioned media	Osaka University	N/A
Y-27632	Sigma Aldrich	Y0503
TrypLE Express	Life Technologies	12605-028
Matrigel Growth Factor Reduced (GFR) Basement Membrane Matrix, Phenol Red-Free, LDEV-Free, 10mL	Corning	356231
Hematoxylin (for general histology)	Thermo Shandon	6765008
Eosin Y alcoholic 0.25% (for general histology)	StatLab	SL98-1
Gill's Hematoxylin (counterstain for ISH)	American Master Tech	HXGHE1GAL
Permanent Mounting Media	Innovex Biosciences	NB300
4', 6-diamidino-2-phenylindole (DAPI)	Sigma Aldrich	D8417-10MG
10% Neutral Buffered Formalin	Fisher Scientific	22-110-869
Hydrogen peroxide solution (30%)	Sigma Aldrich	216763-500ML
Citric acid monohydrate	Sigma Aldrich	C1909-500G
Cytoseal 60	Richard-Allan Scientific	8310-4
Hematoxylin QS (counterstain for IHC)	Vector Laboratories	H-3404
Fluriso (Isoflurane, USP)	VETONE	NDC 13985-030-60
Ketofen (ketoprofen) solution 100 mg/mL	Zoetis	3690385.1
X-tremeGENE9	Sigma	XTG9-RO ROCHE
Retro-X concentrator	Clontech	631455
Polybrene	EMD Millipore	TR-1003-G

(Continued on next page)

Continued

REAGENT or RESOURCE	SOURCE	IDENTIFIER
Primocin	Invitrogen	ant-pm-2
Penicillin/Streptomycin	Thermo Fisher	15140122
Critical Commercial Assays		
Costar 6 Well Clear Flat Bottom Ultra Low Attachment Multiple Well Plates	Corning	3471
Corning BioCoat Matrigel Invasion Chambers with 8.0 μ m PET Membrane in two 24 Well Plates	Corning	354480
ORIS Cell Migration Assay	Platypustech	CMA1.101
TruSeq ChIP Sample Prep Kit	Illumina	IP-202-1012
TruSeq RNA Sample Prep Kit v2	Illumina	RS-122-2001
Nextera DNA Library Prep Kit	Illumina	FC- 121-1030
QIAquick Gel Extraction Kit	QIAGEN	28704
MinElute PCR Purification Kit	QIAGEN	28004
VIEWRNA ISH Tissue Assay kit – 2-Plex (Red-Blue)	Affymetrix	QVT0012
QuantiGene ViewRNA mouse Foxa1 FISH probe	Affymetrix	VB1-16714
Histone Extraction Kit	Abcam	Ab113476
Deposited data		
ChIP-Seq, RNA-Seq, and ATAC-Seq data	This study	GEO: GSE99311
Mouse reference genome NCBI37/mm9	Genome Reference Consortium	https://www.ncbi.nlm.nih.gov/grc/mouse
Human reference genome GRCh37/hg19	Genome Reference Consortium	https://www.ncbi.nlm.nih.gov/grc/human
Microarray	Moffitt et al., 2015	GEO: GSE71729
H3K27ac ChIP-Seq	Diaferia et al., 2016	GEO: GSE64560
H3K27ac ChIP-Seq	Loh et al., 2014	GEO: GSE52657
H3K27ac ChIP-Seq	Abraham et al., 2017	GEO: GSE76783
H3K27ac ChIP-Seq	Christensen et al., 2014	GEO: GSE62412
H3K27ac ChIP-Seq	Lin et al., 2012	GEO: GSE36354
RNA-Seq	Loh et al., 2014	GEO: GSE52657
RNA-Seq	Arda et al., 2016	GEO: GSE57973
Experimental Models: Mouse/Human pancreatic organoids and Cell Lines		
Mouse: N ⁵ Normal pancreatic organoid	Tuveson Laboratory, Boj et al., 2015	N/A
Mouse: N ⁶ Normal pancreatic organoid	Tuveson Laboratory, Boj et al., 2015	N/A
Mouse: P ² PanIN organoid	Tuveson Laboratory, Boj et al., 2015	N/A
Mouse: P ³ PanIN organoid	Tuveson Laboratory, Boj et al., 2015	N/A
Mouse: T ³ Tumor organoid	Tuveson Laboratory, Boj et al., 2015	N/A
Mouse: T ⁶ Tumor organoid	Tuveson Laboratory, Boj et al., 2015	N/A
Mouse: T ¹⁹ Tumor organoid	This paper	N/A
Mouse: T ²³ Tumor organoid	This paper	N/A
Mouse: T ³³ Tumor organoid	This paper	N/A
Mouse: T ³⁴ Tumor organoid	This paper	N/A
Mouse: M ^{1L} Metastatic organoid (liver, paired tumor is T ³)	Tuveson Laboratory, Boj et al., 2015	N/A

(Continued on next page)

Continued

REAGENT or RESOURCE	SOURCE	IDENTIFIER
Mouse: M ^{3L} Metastatic organoid (liver, paired tumor is T ⁶)	Tuveson Laboratory, Boj et al., 2015	N/A
Mouse: M ^{3P} Metastatic organoid (peritoneum, paired tumor is T ⁶)	Tuveson Laboratory, Boj et al., 2015	N/A
Mouse: M ^{6P} Metastatic organoid (peritoneum, paired tumor is T ¹⁹)	This paper	N/A
Mouse: M ^{10P} Metastatic organoid (peritoneum, paired tumor is T ²³)	This paper	N/A
Mouse: M ^{15D} Metastatic organoid (diaphragm, paired tumor is T ³⁴)	This paper	N/A
Mouse: KPC 2D cells (derived from T ³ organoid)	Tuveson Laboratory, Boj et al., 2015	N/A
Human: hN ³⁰ Normal pancreatic organoid (male, 49 years old)	This paper	N/A
Human: hN ³² Normal pancreatic organoid (female, 52 years old)	This paper	N/A
Human: hN ³⁴ Normal pancreatic organoid (male, 24 years old)	This paper	N/A
Human: hT ¹ Tumor organoid (male, 65 years old)	Tuveson Laboratory, Boj et al., 2015	N/A
Human: hT ³ Tumor organoid (male, 35 years old)	Tuveson Laboratory, Boj et al., 2015	N/A
Human: hT ⁷² Tumor organoid (female, 70 years old)	This study	N/A
Human: hT ⁷³ Tumor organoid (male, 76 years old)	This study	N/A
Human: hT ⁸¹ Tumor organoid (male, 66 years old)	This study	N/A
Human: hT ⁸⁵ Tumor organoid (male, 76 years old)	This study	N/A
Human: hT ⁹¹ Tumor organoid (female, 71 years old)	This study	N/A
Human: hT ⁹³ Tumor organoid (male, 55 years old)	This study	N/A
Human: hT ⁹⁴ Tumor organoid (male, 74 years old)	This study	N/A
Human: hT ⁹⁵ Tumor organoid (female, 74 years old)	This study	N/A
Human: hF ² Tumor organoid (female, 60 years old)	This study	N/A
Human: hF ³ Tumor organoid (female, 69 years old)	This study	N/A
Human: hF ²³ Tumor organoid (female, 69 years old)	This study	N/A
Human: hF ²⁴ Tumor organoid (female, 57 years old)	This study	N/A
Human: hF ²⁷ Tumor organoid (male, 54 years old)	This study	N/A
Human: hF ³⁷ Tumor organoid (male, 74 years old)	This study	N/A
Human: hF ³⁹ Tumor organoid (female, 81 years old)	This study	N/A
Human: hF ⁴⁰ Tumor organoid (male, 70 years old)	This study	N/A
Human: hF ⁴¹ Tumor organoid (male, 54 years old)	This study	N/A
Human: hF ⁴² Tumor organoid (female, 71 years old)	This study	N/A
Human: hM ⁶ (F) Tumor organoid (female, 70 years old)	This study	N/A
Human: hT2-2D (derived from hT ² organoid) (male, 47 years old)	This study	N/A
Experimental Models: Organisms/Strains		
Mouse: <i>Kras</i> ^{+/<i>L</i>SL-G12D} ; <i>Trp53</i> ^{+/<i>L</i>SL-R172H} ; <i>Pdx1-Cre</i> (C57BL/6J background)	Tuveson Laboratory, Hingorani et al., 2005	N/A
Mouse: C57BL/6J	The Jackson Laboratory	N/A
Mouse: Crl:NU-Foxn1 ^{nu} , athymic nu/nu mice	Charles River Laboratory	N/A
Oligonucleotides		
shRNA sequences, see Table S6	This study	N/A
qRT-PCR primers, see Table S6	This study	N/A
Genomic DNA-qPCR primers, see Table S6	This study	N/A
sgRNA sequences, see Table S6	This study	N/A

(Continued on next page)

Continued

REAGENT or RESOURCE	SOURCE	IDENTIFIER
<i>Trp53</i> 1loxP PCR primer (Forward) for Figure S1B AGCCTGCCTAGCTTCCTCAGG	Olive et al., 2004	N/A
<i>Trp53</i> 1loxP PCR primer (Reverse) for Figure S1B CTTGAGACATAGCCCACTG	Olive et al., 2004	N/A
Recombinant DNA		
pGCDNsam-Foxa1	Sekiya and Suzuki, 2011	Addgene plasmid ID: #33003
PRRX2-MSCV	Stelnicki et al., 1998	Addgene plasmid ID: #21010
LRG (Lenti_sgRNA_EFS_GFP)	Shi et al., 2015	Addgene plasmid ID: #65656
LRNG (Lenti_sgRNA_EFS_Neo-IRES-GFP)	This study	N/A
MGC Fully Sequenced Mouse <i>Batf2</i> cDNA	GE Healthcare	Clone ID: 4984403
MGC Fully Sequenced Mouse <i>Gata5</i> cDNA	GE Healthcare	Clone ID: 40046620
MGC Fully Sequenced Mouse <i>Pax9</i> cDNA	GE Healthcare	Clone ID: 3707718
MSCV-NIG/empty	This study	N/A
MSCV-NIG/ <i>Batf2</i>	This study	N/A
MSCV-NIG/ <i>Pax9</i>	This study	N/A
MSCV-NIG/ <i>Prrx2</i>	This study	N/A
MSCV-NIG/ <i>Foxa1</i>	This study	N/A
MSCV-NIG/V5- <i>Foxa1</i>	This study	N/A
MSCV-NIG/3xFlag- <i>Gata5</i>	This study	N/A
MSCV-NIG/V5- <i>Gata5</i> -P2A-3xFlag- <i>Gata5</i>	This study	N/A
Software and Algorithms		
ImageJ	NIH	https://imagej.nih.gov/ij/
Metascape	Tripathi et al., 2015	http://metascape.org/gp/index.html#/main/step1/
GENE-E	Broad Institute	https://software.broadinstitute.org/GENE-E/
GREAT	McLean et al., 2010	http://bejerano.stanford.edu/great/public/html/
Bowtie v1.0	Langmead et al., 2009	https://sourceforge.net/projects/bowtie-bio/
Samtools	Li et al., 2009	http://samtools.sourceforge.net/
Tophat	Trapnell et al., 2009	https://ccb.jhu.edu/software/tophat/index.shtml
Cufflinks	Trapnell et al., 2010	http://cole-trapnell-lab.github.io/cufflinks/cuffdiff/
UCSC Genome Browser	UCSC	http://genome.ucsc.edu/
liftOver	UCSC	https://genome.ucsc.edu/cgi-bin/hgLiftOver
BEDtools v2.17.0	Quinlan and Hall, 2010	http://bedtools.readthedocs.io/en/latest/
Transcription factor Affinity Prediction (TRAP)	Thomas-Chollier et al., 2011	http://trap.molgen.mpg.de/cgi-bin/home.cgi/
HOMER v4.9	Heinz et al., 2010	http://homer.ucsd.edu/homer/

CONTACT FOR REAGENT AND RESOURCE SHARING

Further information and requests for resources and reagents should be directed to the Lead Contact, Christopher R. Vakoc (vakoc@cshl.edu).

EXPERIMENTAL MODEL AND SUBJECT DETAILS

Mice

KPC mice (*Kras*^{+/*LSL-G12D*}; *Trp53*^{+/*LSL-R172H*}; *Pdx1-Cre*) have been described previously (Hingorani et al., 2005). KPC mice have been backcrossed onto the C57BL/6J mouse strain obtained from The Jackson Laboratory (stock number 000664). Female 6- to 8-week-old syngeneic C57BL/6J or athymic immune-compromised mice (nu/nu) were purchased from The Jackson Laboratory and Charles River Laboratory, respectively. All mice were housed in specific pathogen free conditions prior to use. Prior to the described studies, mice were regularly monitored and determined to be healthy by the veterinary staff. All animal procedures and studies were conducted in accordance with the Institutional Animal Care and Use Committee (IACUC) at Cold Spring Harbor Laboratory.

Organoids, cell lines and culture conditions

In order to derive primary tumor and metastatic organoid cultures from tumor-bearing KPC mice, primary tumor and metastatic tissues were carefully dissected avoiding adjacent normal pancreas or other tissue contamination (Boj et al., 2015). Dissected tissues were minced with surgical scalpels and incubated in digestion buffer (DMEM, 1% FBS, penicillin, streptomycin, 0.125 mg/mL Collagenase Type XI, 0.125 mg/mL Dispase II) for 2 hr at 37°C with gentle rocking. Digested tissues were further digested with TrypLE for 10 min at 37°C with gentle agitation. Cells were resuspended with Matrigel and plated in ultra-low attachment 24 well plates. Once Matrigel was solidified, pancreatic organoid media was added. Pancreatic organoid media contains advanced DMEM/F12, HEPES 10 mM, Glutamax 1X, A83-01 500 nM, mEGF 50 ng/mL, mNoggin 100 ng/mL, hFGF10 100 ng/mL, Gastrin I 0.01 μM, N-acetylcysteine 1.25 mM, Nicotinamide 10 mM, B27 supplement (1X final), R-spondin conditioned media (10% final). For dissociating organoids into single cell suspension, organoids were incubated in 2 mg/ml dispase followed by 10 min TrypLE incubation. Cells were filtered with 40 μm cell strainer. To generate KPC-2D cell lines from tumor organoid cultures, organoids were dissociated into single cells as described above, resuspended with DMEM supplemented with 10% FBS, penicillin and streptomycin and plated in tissue culture plates. For human samples, tissues were minced and incubated in digestion media (5 mg/mL Collagenase XI, 10 μg/mL DNase I, 10.5 μM Y-27632 in Human complete Feeding Medium) at 37°C with mild agitation for up to 1 hr. Cells were plated with Matrigel and grown in Human complete Feeding Medium (advanced DMEM/F12, HEPES 10 mM, Glutamax 1X, A83-01 500 nM, hEGF 50 ng/mL, mNoggin 100 ng/mL, hFGF10 100 ng/mL, hGastrin I 0.01 μM, N-acetylcysteine 1.25 mM, Nicotinamide 10 mM, PGE2 1 μM, B27 supplement (1X final), R-spondin1 conditioned media (10% final), Afamin/Wnt3A conditioned media (50% final) (Mihara et al., 2016). hT2 organoids were generated from a patient derived xenograft (PDX) obtained from Champions Oncology. Tumor dissociation and organoid culture was performed as described above. To establish a 2D culture, organoids were seeded in a 6-well plate with RPMI, 10% FBS, and 1X Penicillin/Streptomycin and allowed to form a confluent monolayer. Human PDA cell line, MiaPaCa-2 was obtained from ATCC. Organoid cultures and cell lines were regularly verified to be free of mycoplasma contamination. The genotype of murine organoids and organoid-derived cell lines was authenticated by PCR-based DNA genotyping.

Human specimens

Normal pancreatic tissue was obtained from islet transplant programs at the University of Illinois at Chicago and University of Miami Miller School of Medicine as described previously (Boj et al., 2015). Pancreatic cancer tissue was obtained from patients undergoing surgical resection or tissue biopsy at Memorial Sloan Kettering, Stony Brook University (GI biobank), Johns Hopkins University, Weill Cornell University, University of California Davis, Thomas Jefferson University Hospital, and Champions Oncology. Human liver metastasis tissue was obtained from Rapid Autopsy Program at University of Nebraska Medical Center. All tissue donations and experiments were reviewed and approved by the Institutional Review Board of Cold Spring Harbor Laboratory and all clinical institutions. Written informed consent was obtained prior to acquisition of tissue from all patients. Samples were confirmed to be tumor or normal based on pathologist assessment. For the patients included in this study 36% were female, 52% were male, 12% were undetermined and the median age was 69 years old.

METHOD DETAILS

Next-generation sequencing library constructions

Chromatin immunoprecipitation (ChIP) assay

For ChIP experiments with PDA organoids, organoids were dissociated into single cells to yield 10⁶ cells as described above. For ChIP experiments with KPC-2D cells, cells were trypsinized into single cells to yield 5 × 10⁶ cells. Cells were crosslinked for 10 min at room temperature with formaldehyde (1% final) and then quenched with 0.125 M glycine for 10 min. PBS-washed cells were then lysed with 200 μl of Cell lysis buffer (10 mM Tris-Cl pH 8.0, 10 mM NaCl, 0.2% NP-40) with protease inhibitor and incubated for 10 min at 4°C. Chromatin was isolated by centrifugation at 7,400 rpm for 30 s and pellets were lysed with 200 μL of Nuclei lysis buffer (50 mM Tris-Cl pH 8.0, 10 mM EDTA, 1% SDS) with protease inhibitor followed by incubation for 10 min at 4°C. Lysed chromatin was then sonicated for 10 cycles (30 s on/ 30 s off, low amplitude) using Bioruptor (Diagenode). After sonicated chromatin was centrifuged at 14,000 rpm for 10 min at 4°C, the supernatants were incubated for 1 hr with 800 μL of IP dilution buffer (20 mM Tris-Cl pH 8.0, 2 mM EDTA, 150 mM NaCl, 1% Triton X-100, 0.01% SDS), 10 μg of rabbit IgG and 50 μL of Protein A magnetic beads for pre-clearing sheared chromatin. Immunoprecipitation was further performed with 1 mL of pre-cleared chromatin, 2 μg of antibody and

20 μ L of Protein A magnetic beads overnight at 4°C with rotation. Next day, immunocomplexes were washed as follows – first wash once with IP Wash I buffer (20 mM Tris-Cl pH 8.0, 2 mM EDTA, 50 mM NaCl, 1% Triton X-100, 0.1% SDS), second wash twice with High salt buffer (20 mM Tris-Cl pH 8.0, 2 mM EDTA, 500 mM NaCl, 1% Triton X-100, 0.01% SDS), third wash once with IP Wash II buffer (10 mM Tris-Cl pH 8.0, 1 mM EDTA, 0.25 M LiCl, 1% NP-40, 1% Na-deoxycholate) and final wash twice with TE pH 8.0. The washed immunocomplexes were eluted with 200 μ L of elution buffer (1% SDS, 0.1 M NaHCO₃) at 45°C for 30 min and reverse-cross-linked with RNase A (1 μ g/ μ l) and 0.25 M NaCl overnight at 65°C water bath. Next day, immunoprecipitated DNA was treated with Proteinase K (0.2 mg/ml) for 2 hr at 45°C and purified with QIAquick gel extraction kit in 55 μ L of EB elution buffer.

ChIP-seq library construction

ChIP-seq libraries were constructed using the TruSeq ChIP Sample Prep Kit (Illumina) according to the manufacturer's instructions. Briefly, 50 μ L of purified ChIP DNA was end-repaired for dA-tailing, followed by adaptor ligation. Adaptor-ligated ChIP-DNA was size-selected (250 – 300 bp) via agarose-gel electrophoresis, gel-extracted with QIAquick gel extraction kit and used for 15 cycles of PCR amplification. Amplified DNA was finally size-selected with SPRI clean-up by AMPure XP beads (1:1). Quality of ChIP-seq library was determined by Bioanalyzer using the High Sensitivity chip (Agilent) and the average size of ChIP-seq libraries ranged from 250 to 350 bp. For multiplexing, equal molar quantities of libraries were combined by considering sequencing depth per sample (20 to 40 million reads per library). ChIP-seq libraries were sequenced using an Illumina HiSeq2500 or NextSeq platform with single-end reads of 50 bases.

RNA-seq library construction

For RNA-seq experiments with PDA organoids, organoids were dissociated into single cells to yield 5×10^5 cells. For KPC-2D cells, cells were trypsinized into single cells to yield 2×10^6 cells. Total RNA was extracted with TRIzol reagent (Thermo Fisher) according to the manufacturer's instructions. Briefly, cells were lysed with 1 mL of TRIzol and 200 μ L of chloroform, followed by incubation for 10 min at 4°C. After centrifuging lysed RNA at 12,000 g for 10 min at 4°C, the supernatants were incubated with the same volume of 2-isopropanol for 15 min at room temperature. RNA was precipitated at 10,000 g for 10 min at 4°C, washed with 75% EtOH in DEPC-treated water and eluted in RNase-free water. RNA-seq libraries were constructed using the TruSeq sample Prep Kit V2 (Illumina) according to the manufacturer's instructions. Briefly, 2 μ g of purified RNA was poly-A selected and fragmented with fragmentation enzyme. After first and second strand synthesis from a template of poly-A selected/fragmented RNA, other procedures from end-repair to PCR amplification were done according to ChIP-seq library construction steps. Quantity of RNA-seq library was determined by Nanodrop, and average quantity of RNA-seq libraries ranged from 40 to 80 ng/ μ l. Multiplexing for sequencing was performed as described for ChIP-seq library construction. RNA-seq libraries were sequenced using an Illumina HiSeq2500 or NextSeq platform with single-end reads of 50 bases.

ATAC-seq library construction

ATAC-seq library construction was performed as previously described with minor modifications (Buenrostro et al., 2013). For ATAC-seq experiments with PDA organoids, organoids were dissociated into single cells to yield 50,000 cells and lysed with 50 μ L of Lysis buffer (10 mM Tris-Cl pH 7.4, 10 mM NaCl, 3 mM MgCl₂, 0.1% NP-40, 0.1% Tween-20, protease inhibitor) and incubated for 5 min at 4°C. After centrifuging at 6,000 g for 10 min at 4°C, pellets (nuclei) were resuspended with 50 μ l of transposition mix (Illumina; 1X Tagment DNA buffer, Tn5 Transposase, 0.05% Tween-20, nuclease-free DW) and incubated for 30 min at 37°C in the Thermomixer by shaking at 300 rpm. Transposition was terminated by adding 50 mM EDTA, followed by quenching excessive EDTA with 45 mM MgCl₂. Transposed DNA was purified using QIAgen MinElute columns, subsequently amplified with Nextera sequencing primers and NEB high fidelity 2X PCR master mix for 12 cycles (New England Biolabs). PCR-amplified DNA was purified using QIAgen MinElute columns and sequenced using NextSeq platform with single-end reads of 50 bases.

Protein and DNA/RNA-related experiments

Cloning

Foxa1 cDNA (Addgene #33003) (Sekiya and Suzuki, 2011), Gata5 cDNA (GE Healthcare, Clone ID: 40046620), Prrx2 (Addgene #21010) (Stelnicki et al., 1998), Batf2 (GE Healthcare, Clone ID: 4984403) and Pax9 (GE Healthcare, Clone ID: 3707718) cDNA were subcloned into MSCV-PGK-Neo-IRES-GFP. The amino acid sequences for P2A linker; GSG-ATNFSLLKQAGDVEENPGP. miR30-based shRNAs were designed and cloned as previously described (Fellmann et al., 2013). Sequence information for shRNAs can be found in Table S6.

CRISPR-mediated genome editing in organoids

Guide RNAs were designed using CRISPR Design (<http://crispr.mit.edu>). gRNAs were cloned into LRG vector (Addgene #65656) (Shi et al., 2015) or LRNG vector. LRNG vector was generated by inserting Neo-IRES cassette in front of GFP cassette in LRG vector. Lenti-Cas9-Blasticidin or Lenti-Cas9-Puro was lentivirally introduced into T or M organoids. After antibiotics selection, gRNA was lentivirally introduced. For *Trp53* inactivation in T organoids, LRNG-sgTrp53 introduced cells were selected with G418 (1 mg/mL). For DNA-binding domain mutation of *Foxa1* in M organoids, LRNG-sgFoxa1 introduced cells were sorted by GFP positivity with flow cytometry. To validate CRISPR-Cas9 mediated mutation efficiency, genomic DNA (~500bp) containing sgRNA binding region was PCR amplified from total genomic DNA. For qPCR-based quantification of editing efficiency, pairs of primers proximal to PAM sequence of each gRNA were designed. Relative efficiency for genomic DNA amplification was measured by qPCR-based 2(delta)(delta)CT method, compared to sgRosa expressing cells as a control.

Genomic DNA isolation from organoids

Organoids were harvested from two wells of 24 well plate and centrifuged with 10,000 g for 1 min at 4°C. Cell pellets were resuspended with 40 μ l of lysis buffer (10 mM Tris-HCl, 50 mM KCl, 2.5 mM MgCl₂, 0.45% Nonidet P-40, 0.45% Tween20 and 60 μ g/mL Proteinase K) and incubated at 55°C for 1 hr and subsequently at 96°C for 10 min. 1 μ l of crude DNA extract was used for further genotyping analysis.

Western blotting

For western blotting experiments with PDA organoids, organoids were dissociated into single cells to yield 5×10^5 cells. For western blotting experiments with KPC-2D cells, cells were trypsinized into single cells to yield 5×10^5 cells. To prepare whole-cell lysates, cell pellets were directly lysed with 100 μ l of PBS, 100 μ l of 2x Laemmli buffer (BIO-RAD) and 4 μ l of 2-Mercaptoethanol. Extracts from 30,000 - 50,000 cells were loaded into each lane of SDS-PAGE gel electrophoresis, followed by transfer to nitrocellulose for immunoblotting.

Extraction of total histones

500,000 cells were prepared from each organoids as described above, and proceeded to isolate total histones with Histone Extraction Kit (Abcam, ab113476) according to manufacturer's protocol.

cDNA synthesis and qRT-PCR

Using TRIzol reagents according to the manufacturer's instructions, total RNA was extracted as described in RNA-seq experiments. DNase I treatment was subsequently performed to eliminate contaminating genomic DNA upon RNA isolation. cDNA was synthesized with Q-script cDNA SuperMix (Quanta Bio), which primes RNA with a blend of random hexamer and oligo-dT. All results were quantified by qPCR performed using power SYBR green (Thermo Fisher) on an ABI 7900HT (ABI) and quantified using the $2^{-(\Delta\Delta CT)}$ method with housekeeping gene *Gapdh* as the control gene for internal normalization. All qPCR primer sequences used in this study are listed in the [Table S6](#).

Cell culture-related experiments

Retrovirus/lentivirus production and infection of organoids

Retrovirus was produced in ecotropic Phoenix cells by transfecting plasmids with X-tremeGENE9 transfection reagent. Ecotropic Phoenix cells were plated a day before transfection with 70%–80% confluency in 10 cm tissue culture plate. Media was changed with 9.6 mL of antibiotic-free DMEM supplemented with 10% FBS. 10 μ g of plasmid DNA and 15 μ l of X-tremeGENE9 reagent was mixed in 400 μ l of DMEM and incubated for 20 min at room temperature. Transfection mixture was added to the cells. After 24 hr, media was removed and fresh DMEM supplemented with 10% FBS was added. Retrovirus-containing supernatant was harvested at 48 hr and 72 hr after transfection and filtered through a 0.45 μ m filter. To concentrate retrovirus, one volume of Retro-X™ concentrator with 3 volumes of supernatant was mixed and incubated at 4°C overnight. After centrifugation at 1,500 x g for 45 min at 4°C, the virus pellet was resuspended with organoid media (10 times concentrated from the initial volume). To infect organoids with retrovirus, organoid cultures were dissociated into single cells as described above and spinoculated by centrifugation. In brief, 100,000 cells were mixed with 500 μ l of concentrated virus, supplemented with polybrene (final concentration; 8 μ g/mL) and placed in a 24 well low-attachment plate. The plate was centrifuged with 600 x g for 1 hr at room temperature, and incubated at 37°C CO₂ incubator for 6 hr. Then, cells were resuspended with 200 μ l of Matrigel, plated in 4 wells of 24-well plate and grown as organoids. Two days after infection, G418 (1 mg/mL, final concentration), puromycin (2 μ g/mL, final concentration) or blasticidin (10 μ g/mL, final concentration) was added for antibiotic selection.

Lentivirus was produced in 293T cells by transfecting plasmids and packaging plasmids (pMD2 and psPAX2) with X-tremeGENE9 transfection reagent. To concentrate lentivirus, Lenti-X™ concentrator was used. All other procedures were done as described for retrovirus production.

Retrovirus production and infection of KPC-2D cells

For retroviral packaging, Plat-E cells were used for the transient transfection with PEI (polyethyleneimine) according to standard protocols. The viral supernatants were harvested twice at 48 and 72 hr post-transfection and cell debris removed from the supernatant using 0.45 μ m filter prior to transduction of KPC-2D cells. To maximize transduction efficiency, polybrene (10 μ g/mL) was supplemented during retroviral infection. Two days after infection, G418 (1 mg/mL, final concentration) was added for antibiotic selection.

Boyden chamber-invasion assay

For in vitro invasion assay, BioCoat Matrigel invasion chambers with 8.0 μ m PET membrane in 24-well plates (Corning) were used. Once invasion chamber was thawed, 500 μ l or 800 μ l of serum-free DMEM was added to the interior of insert and the bottom of the well, respectively. After incubating for 2 hr in a tissue culture incubator for rehydration, KPC-2D cells (50,000 cells) were resuspended in 500 μ l of serum-free DMEM and added to the upper chamber. In the lower chamber, 800 μ l of DMEM with 10% FBS was added as a chemoattractant. After 24 hr of incubation in a tissue culture incubator, the upper well containing membrane was scrubbed carefully several times with a cotton swab soaked in PBS to remove non-invaded cells. The lower membrane of the well was rinsed with PBS carefully several times. Invaded cells were stained with Syto13 (Thermo Fisher, 1:10,000 in PBS) for 15 min in the dark, and pictures were taken under a 4x GFP fluorescence microscope for counting. Invasion was calculated as the average number of cells per 4x field, determined by ImageJ software (NIH).

Anchorage-independent sphere culture

KPC-2D cells (25,000 cells) were resuspended in 1.5 mL of serum free DMEM supplemented with 20 μ l/mL B27, 20 ng/mL EGF and 20 ng/mL bFGF in ultra-low attachment 6-well plates (Corning). Every 3 days, 200 μ l of fresh media was added. Spheres grown in anchorage-independent condition (or tumor spheres) were photographed at day 14 under a 4x microscope with the bright-field. Before taking pictures, cells were gently transferred from 6-well to 24-well plate, to increase the density of spheres per well. Sphere sizes were determined by ImageJ software (NIH).

Clonogenic growth assay

KPC-2D cells (1,000 cells) were resuspended in DMEM with 10% FBS, then plated in regular 6-well plates. Colonies were briefly stained with 0.05% crystal violet in 95% EtOH and washed slowly running water from the tap. Images of plates were taken with a gel documentation system. Clonogenic growth was calculated as the average % area of colonies per well, determined by ImageJ software (NIH).

Cell migration assay

KPC-2D cells (300,000 cells) were resuspended in 100 μ l of DMEM and incubated with an ORIS insert in a 96-well plate to allow attachment overnight (Platypustech). Next day, the insert was removed using a stopper tool to reveal a migration zone of 2 mm diameter. In a control well, the insert was left in as a pre-migration control. Once wells were gently washed with PBS, 100 μ l of fresh media was added to allow migration overnight. Next day, wells were gently washed with PBS and stained with Syto13 (Thermo Fisher, 1:10,000 in PBS) for 15 min in the dark and images were taken under a 4x GFP fluorescence microscope for counting. Migration was calculated as the average number of cells in 2 mm-migration zone, determined by ImageJ software (NIH).

Generation of T organoid clones with Trp53 LOH

Two gRNAs targeting the first and second intron of *Trp53* locus were lentivirally introduced in Cas9 expressing T organoids. First intron targeting gRNA was designed to recognize only WT allele due to the loxP sequence in *Trp53* mutant allele. After introduction of the two gRNAs in LRNG vector followed by G418 selection (1 mg/mL) for 4 days, single cell dissociated organoids were grown in DMEM supplemented with 10% FBS and penicillin/streptomycin for 2 days. Single cell-derived organoids were dissolved in 10 mL of ice-cold PBS, manually picked under the microscope, transferred to fresh Matrigel and expanded in organoid media. Absence of WT *Trp53* was further validated by PCR genotyping and Sanger sequencing of *Trp53* cDNA.

In vivo experiments

In vivo transplantation assays

For orthotopic, intraperitoneal, intrasplenic and subcutaneous injections, mice were anesthetized using an automatic delivery system (Isoflurane Vaporizer). Iodine solution was applied to the surgery site. For orthotopic or intraperitoneal injection, a small incision (~1 cm) in the skin of the upper left quadrant of the abdomen was made. Cells were resuspended with 50 μ l of Matrigel and injected into the parenchyma of the pancreas or peritoneal wall, respectively.

Intrasplenic injection of cancer cells for modeling hepatic metastases has been described in detail elsewhere (Soares et al., 2014). Briefly, the spleen was divided by placing two ligating clips (Teleflex, #002200) in the center of the spleen, and cells resuspended with 200 μ l PBS were slowly injected into the exposed hemispleen. By applying a ligating clip (Teleflex, #001200) to the most distal aspect of pancreas and splenic vessels, the pancreas and splenic vessels were ligated by cutting above the clips. An incision at the peritoneal cavity was sutured using Coated Vicryl suture (Johnson & Johnson, J392H) and stainless steel wound clips (Reflex7, CellPoint Scientific, Inc. #203-1000) were applied to the skin. For the subcutaneous injection, mice were anesthetized as described above. Cells resuspended with 50 μ l of Matrigel were injected into the subcutaneous space of the left flanks. One flank per mouse was injected. For tail vein injection, mice were restrained and cells (resuspended in 200 μ l of PBS) were injected intravenously through the tail vein.

For portal vein injection, dissociated organoid cells (5×10^5) resuspended in sterile phosphate buffered saline (PBS, 100 μ l) were injected in the portal vein of 10-week-old male C57BL/6 mice (Charles Rivers Laboratories): a midline incision was made through skin and peritoneum cutting from the xiphoid process and 10-15 mm caudal. The intestine was gently displaced on sterile gauze to reveal the portal vein. Cells were injected directly into the portal vein and Gelfoam sterile Compressed Sponge (Pfizer) was kept on the injection site until achieving hemostasis. The intestine was returned to the abdominal cavity and the incisions in peritoneum and skin closed by sutures. Four weeks after injection, mice were transcatheterially perfused with PBS followed by 4% PFA solution in PBS. Livers and lungs were harvested and processed for paraffin embedding.

Human tissue microarrays

Human tissue microarrays containing primary tumors and metastases were obtained from Rapid Autopsy Program at University of Nebraska Medical Center. Human pancreatic, metastatic, and unaffected specimens from decedents who have previously been diagnosed with pancreatic ductal carcinoma were obtained from the University of Nebraska Medical Center's Tissue Bank through the Rapid Autopsy Pancreatic program in compliance with IRB 091-01. To ensure minimal degradation of tissue, organs were harvested within three hours post mortem and the specimens placed in formalin for immediate fixation. The tissue microarrays were made from paraffin blocks of formalin fixed tissue from rapid autopsies. Large 2.0 and/or 3.0 mm cores were used to construct the tissue arrays. The cores were imbedded in agarose recipient blocks (Tissue-Tek® Quick-Ray). The tissue microarray blocks were cut into 4 μ m thick sections and mounted on charged slides.

Histology

Lung tissues were perfused by intratracheal injection of 10% neutral buffered formalin (NBF) and postfixed with 10% NBF overnight. All other tissues were fixed with 10% NBF overnight. Tissues were processed with standard tissue processing protocol, embedded in paraffin and 6 μ m sections cut. Formalin fixed paraffin-embedded (FFPE) tissue sections were stained with hematoxylin and eosin, or used for immunohistochemical staining and RNA fluorescence in situ hybridization.

Immunohistochemistry

FFPE sections were deparaffinized and rehydrated. For antigen retrieval, slides were incubated with boiling 0.01 M Citrate buffer (pH 6.0) for 20 min. Endogenous peroxidase activity was quenched in 3% H₂O₂. Section were incubated with goat polyclonal anti-Foxa1 antibody (1:200) overnight at 4°C. Antibody was visualized by ImmPRESS™ HRP Anti-Goat IgG (Peroxidase) Polymer Detection kit and ImmPACT DAB Peroxidase (HRP) Substrate. Cover slides were mounted with Cytoseal 60.

RNA Fluorescence in situ hybridization (FISH)

RNA FISH was performed according to ViewRNA ISH Tissue 2-Plex Assay (Affymetrix) manufacturer's protocol using 10 min pre-treatment and 10 min protease treatment. In brief, RNA FISH was performed on freshly prepared FFPE tissue sections. Mouse *Foxa1* (VB1-16714, type 1) was used. 4', 6-diamidino-2-phenylindole (DAPI) was used for counterstaining. Cover slides were mounted with Permanent Mounting Media. Images were taken with a Leica SP8 confocal microscope (Leica Biosystems).

Quantification

In brief, H&E slides were scanned in Aperio scanoscope and analyzed by Aperio Imagescope software. To quantify lung metastasis, clusters of cells with abnormal nuclei were defined as metastasis. Among lung lobes, the biggest and a representative lobe was chosen. For the percentage area of each metastasis, area of metastatic lesions was divided by total area. The number of metastatic nodules per entire lung lobes was also counted. H&E slides of lung and liver tissues were examined for micrometastases. Metastasis frequency was represented as the percentage of mice with macroscopic or microscopic metastases in each cohort. To measure tumor weight from orthotopic, subcutaneous and intra-peritoneal wall injections of organoids, tumor tissues were harvested from the sacrificed mice. Adjacent non-tumor tissues were carefully removed from tumor using scalpel and tumor weight was measured.

Computational analyses

Alignment of ChIP-seq and ATAC-seq reads

Raw reads from fastq files were aligned to the reference mouse genome assembly mm9 using Bowtie with defaults except allowing two-mismatches for only unique alignment; -v 2 -m 1 (Langmead et al., 2009). To avoid clonal artifacts introduced in the library amplification steps, duplicated mapped reads were further removed using Samtools (Li et al., 2009). Finally, bam files were subjected to other analyses with HOMER suites (Heinz et al., 2010).

Identification of ChIP-seq enriched peaks

Processed bam files were subjected to identify peaks and calculate ChIP-seq tags using findPeaks tool with the parameter of finding histone-enriched regions (-style histone). Once ChIP-seq peaks were identified from 16 different organoids (N, P, T and M), mergePeaks tool with default setting (maximum distance between peak centers to merge: 100 bp) was used to combine all peaks, and yielded union of ChIP-seq peaks (ALL regions, n = 34,852). Once union of peaks were identified, ChIP-seq tags were re-calculated at a given interval by normalizing to a read depth of 10 million tags with annotatePeaks tool.

Identification of 857 GAIN regions

From 34,852 union peaks of H3K27ac ChIP-seq in organoids, relative fold changes of each H3K27ac peaks from P, T and M organoids were calculated by comparing with averaged H3K27ac signals of two N organoids (N^{av9}: average of N⁵ and N⁶). With this, 857 peaks (GAIN regions) were defined as the union of H3K27ac peaks - more than 10-fold increase of H3K27 signal in any of P, T and M organoids compared to N^{av9}.

Displaying ChIP-seq and ATAC-seq data

To generate browser tracks for visualizing with UCSC genome browser, the makeBigWig tool was used. To create a metagene plot or heatmap-density plot, the annotatePeaks tool was used by centering ChIP-seq or ATAC-seq regions extended to \pm 5,000 bp (H3K27, H3K4me1 ChIP-seq and ATAC-seq), or \pm 2,500 bp (FOXA1) with 25 bp bins.

Quantitative analysis of ChIP-seq and ATAC-seq meta-profiles

To measure differential enrichment from ChIP-seq or ATAC-seq meta-profiles, 2-kb from peaks center (H3K27ac and H3K4me1 ChIP-seq) or 1-kb from peaks center (FOXA1 ChIP-seq and ATAC-seq) were compared. From each bin of the given regions described above, average signals were calculated (81 bins for 2-kb and 41-bins for 1-kb regions, including a bin of center) and compared. Kolmogorov-Smirnov test was used to obtain *p* value from above comparisons of distribution.

Motif enrichment in GAIN regions

To find enriched motifs in GAIN regions, the 1-kb from the center of GAIN regions was used to extract genomic sequences from the mm9 genome using UCSC table browser. These genomic sequences were further analyzed with TRAP algorithm to identify enriched motifs, compared to JASPAR vertebrates with mouse promoters as the control, and Benjamini-Hochberg as the correction (Thomas-Chollier et al., 2011). To further calculate the actual enrichment of given motif in GAIN regions, the intervals of putative motif binding sites were predicted with TRAP (weight score threshold is 5.0) and intersected with GAIN regions using BEDtools (Quinlan and Hall, 2010). If there was more than 1-bp overlap, the given interval of motif was considered as GAIN regions-overlapping.

Gene ontology (GO) analysis of genes associated with GAIN regions

Genes associated with *GAIN* regions were determined by GREAT tool with a default setting (basal plus extension) (McLean et al., 2010). A list of the defined genes was then used as an input for GO analysis with Metascape tool (Tripathi et al., 2015), further ranked by $-\log_{10} p$ value to reveal top GO terms in Figure S2M.

ChIP-seq peak annotation

To annotate ChIP-seq peaks, the annotatePeaks tool was used to determine whether a peak was in the TSS (transcription start site), TTS (transcription termination site), exon (Coding), 5' UTR exon, 3' UTR exon, intronic, or intergenic. In this study, 5' UTR and 3' UTR exons were unified as exon.

Analysis of publicly available ChIP-seq data

To analyze publicly available ChIP-Seq data, each SRA files were downloaded from NCBI Gene Expression Omnibus (<https://www.ncbi.nlm.nih.gov/geo/>), and analyzed with same ChIP-Seq analysis pipeline used in this study.

Identification of GAIN regions in human genome

To identify *GAIN* regions in human genome, 857 genomic annotations of *GAIN* regions defined in mouse genome assembly (mm9) were converted to human genome assembly (hg19) using lift Over tool of UCSC genome browser (<http://genome.ucsc.edu/cgi-bin/hgLiftOver>). To match the sequences of *GAIN* regions between mouse and human assembly, 20-bp center of 857 *GAIN* regions were used with minimum ratio of bases that must remap as 0.1 (default), which yielded 475 *GAIN* regions of hg19 assembly.

ChIP-Seq analysis of GAIN regions in non-pancreatic cancer

To analyze H3K27ac or H3K4me1 signals at *GAIN* regions in non-pancreatic human cancer cells, genomic annotations of *GAIN* regions converted to hg19 assembly as described above were used. Non-pancreatic cancer cells with its H3K27ac ChIP-Seq dataset deposited in NCBI GEO database are listed as follows (cancer type-cell line-Sequence Read Archive (SRA) name): T-ALL_MOLT4: SRR3098559, T-ALL_MV4-11: SRR3098560, Neuroblastoma_NB1643: SRR3098561, Neuroblastoma_NGP: SRR3098562, T-ALL_P12-ICHIKAWA SRR3098563, T-ALL_PEER SRR3098564, B-ALL_SEM SRR3098566, NSCLC_H82 SRR1613966, NSCLC_GLC16 SRR1613964, Multiple myeloma_MM1S SRR444454 (available from NCBI GEO: GSE76783, GSE62412, GSE36354).

Differential gene expression of RNA-seq

Raw reads from fastq files were aligned to the reference mouse genome assembly mm9 using Tophat allowing no mismatch (Trapnell et al., 2009). Differentially expressed genes were analyzed using Cufflinks tools, by masking structural RNAs (e.g., ribosomal or mitochondrial RNA) to keep total reads-based normalization from undesired effect by heavily mapped reads (Trapnell et al., 2010). From all annotated genes, two filtering steps were followed to define expressed genes in organoids. First, all miRNAs and snoRNAs were manually excluded from a list of annotated genes to focus on protein-coding genes. Second, genes were removed if the rpkm status of Cufflink output is other than 'OK' in any of 16 organoids (N, P, T and M) as they are likely to have low reads depth to assign the genes. With this, 14,007 genes expressed in organoids were defined.

Unsupervised hierarchical clustering analysis

To cluster organoids based on similar matrix in ChIP-seq or RNA-seq datasets, GENE-E tool was used (broadinstitute.org). Similarity was determined by Spearman correlation coefficients with average-linkage clustering method.

Gene set enrichment analysis

Gene set enrichment analyses (GSEA) were performed according to the instructions. To generate a custom gene set for *GAIN* regions, genes with the closest TSS from 857 *GAIN* regions were assigned as peak-associated genes. Gene sets for human PDA signatures and posterior foregut development signature were obtained from previous studies (Loh et al., 2014; Moffitt et al., 2015).

QUANTIFICATION AND STATISTICAL ANALYSIS

Statistical significance for all experiments was evaluated by comparing p values determined by Prism software with unpaired two-tailed Student t test, except for meta-profile comparisons with Kolmogorov-Smirnov test.

DATE AND SOFTWARE AVAILABILITY

The accession number for the data for ChIP-seq, RNA-seq, and ATAC-seq reported in this study is NCBI GEO: GSE99311.

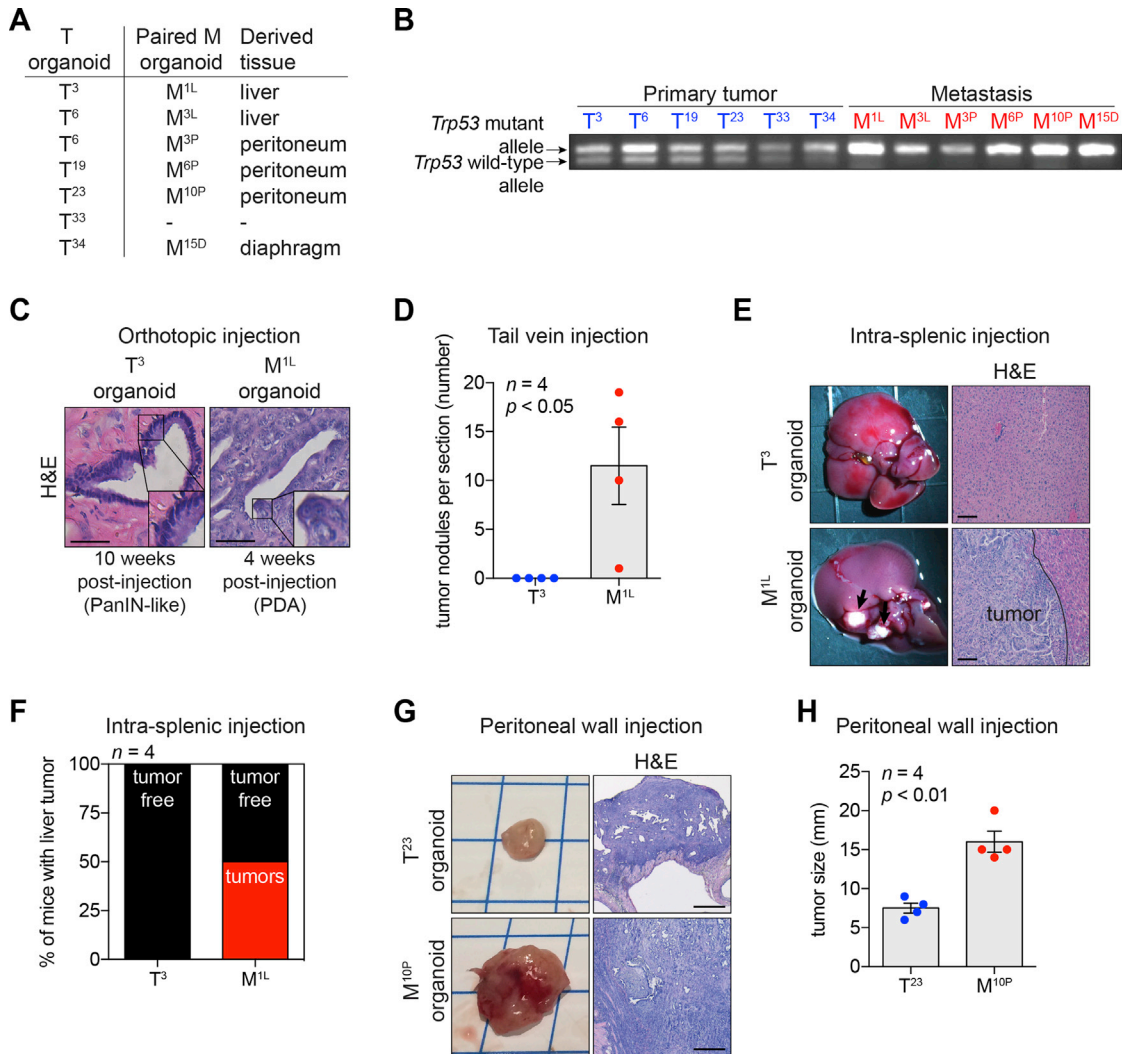


Figure S1. Modeling and Characterization of Primary Tumor- and Metastasis-derived Murine PDA Organoids, Related to Figure 1

(A) Table shows six pairs of matched primary tumor- and metastasis-derived organoids used in this study.

(B) PCR-based genotyping for assessing loss-of-heterozygosity of the *Trp53* allele in T and M organoids used in this study.

(C) Representative images of H&E staining of orthotopic transplants of T³ or M^{1L} organoids in C57BL/6J mice. Mice were sacrificed at the indicated time after injection. Insets show higher magnification of the indicated area. Scale bars, 100 μ m.

(D) Quantification of the number of lung tumor nodules per section after tail vein injection of indicated organoids (n = 4).

(E and F) Representative bright field images (E, left) and H&E staining (E, right) of liver and percentage of mice with liver tumor (F) 2 months after intra-splenic injection of T³ and M^{1L} organoids (n = 4) in C57BL/6J mice. Scale bars, 100 μ m.

(G-H) Representative bright field images (G, left) and H&E staining (G, right) of tumors and quantification of the peritoneal tumor size (H) after peritoneal wall injection of indicated organoids (n = 4). Scale bars, 500 μ m.

For bar charts, each dot represents a mouse and the mean \pm SEM is shown. *p* value was determined by Student's *t* test.

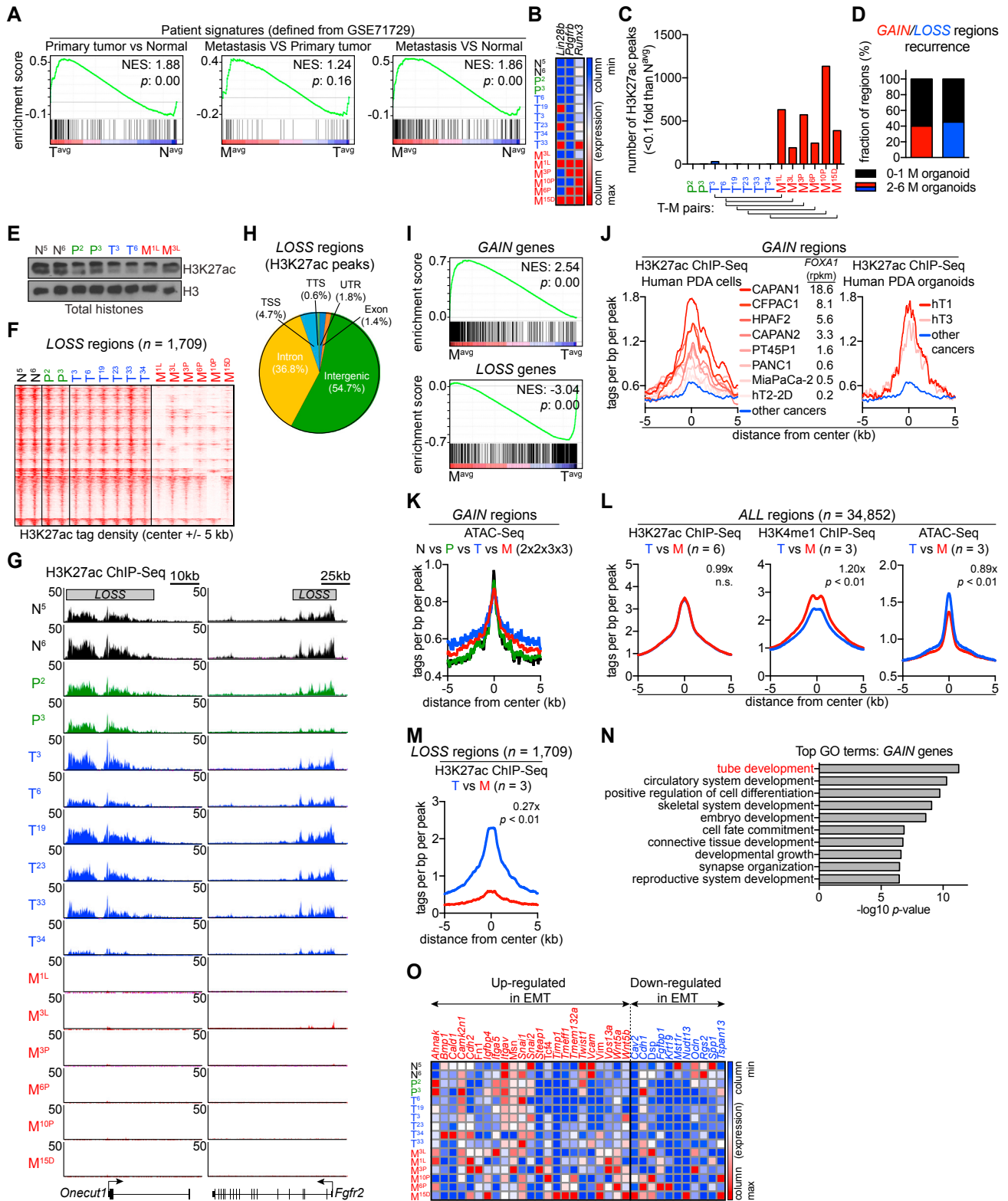


Figure S2. Enhancer Landscape and Gene Expression Profiling in PDA Progression, Related to Figure 2
 (A) GSEA-based comparison of patient- and organoid-derived gene expression profiles at matched stage of PDA progression.
 (B) Column-normalized heatmap representation of known drivers of PDA metastasis in N, P, T and M organoids.

(legend continued on next page)

-
- (C) Number of H3K27ac peaks decreased more than 10-fold relative to N^{avg} in the indicated organoids.
- (D) Recurrence of *GAIN* and *LOSS* regions in M organoids. Fraction of *GAIN* or *LOSS* regions that are present in more than two M organoids is shown as red or blue, respectively.
- (E) western blot analysis of H3K27ac in total histones from the indicated organoids.
- (F) Heatmap representation of *LOSS* regions based on H3K27ac occupancy in organoids. The 1,709 *LOSS* regions were identified from the union of all gained H3K27ac peaks described in Figure 2B. 10-Kb around the center of *LOSS* regions are displayed for each organoid. Each row represents a single region (n = 1,709). Each column represents an individual organoid (n = 16).
- (G) Representative H3K27ac ChIP-seq profiles of *LOSS* regions at *Onecut1* and *Fgfr2* loci in N, P, T and M organoids.
- (H) Pie chart showing the genomic annotations of 1,709 *LOSS* regions according to the location of a given peak. TSS, '-1-kb to +100-bp' of transcription start sites. TTS, '-100-bp to +1-Kb' of transcription termination sites. UTR includes both 5' and 3' UTRs.
- (I) GSEA of averaged M^{avg} versus averaged T^{avg} RNA-seq using *GAIN* (top) and *LOSS* genes (bottom).
- (J) Metagene representation of H3K27ac signal in *GAIN* regions of human PDA cell lines (left) and patient-derived PDA organoids (right). Other cancers include 6 leukemia, 2 neuroblastoma and 2 non-small cell lung cancer cell lines (Abraham et al., 2017; Christensen et al., 2014; Lin et al., 2012).
- (K) Metagene representation of the mean ATAC-seq signal at *GAIN* regions in the indicated organoids.
- (L) Metagene representation of the mean ChIP-seq signal for H3K27ac (left), H3K4me1 (middle) and ATAC-seq (right) at *ALL* regions in the indicated organoids.
- (M) Metagene representation of the mean ChIP-seq signal for H3K27ac at *LOSS* regions in the indicated organoids.
- (N) Gene ontology (GO) analysis of genes proximal to 857 *GAIN* regions with Metascape. Default gene regulatory domain definition of GREAT tool (basal plus extension) was used to assign *GAIN* regions-associated genes, which yielded 1,090 genes. Only the top 10 GO terms ranked by their significance (*p* value) are shown.
- (O) Column-normalized heatmap representation of epithelial-mesenchymal transition (EMT)-related gene in N, P, T and M organoids. Each row represents an indicated organoid, and each column represents an individual EMT-related gene; genes indicated as red are known to be upregulated during EMT, and genes indicated as blue are known to be downregulated during EMT.

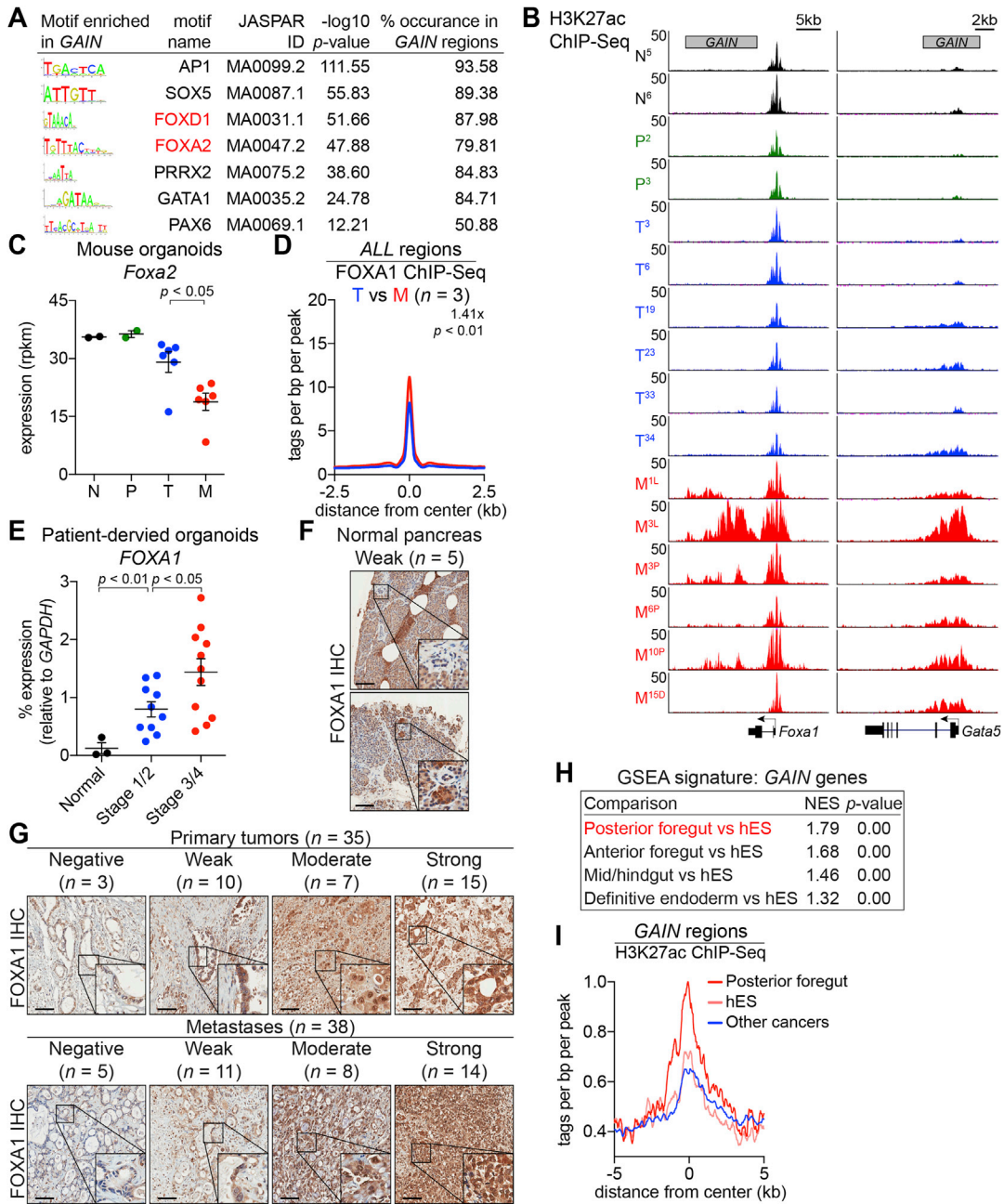


Figure S3. Association of *GAIN* Regions and Posterior Foregut Enhancers, Related to Figure 3

(A) Representation of motifs enriched in *GAIN* regions, related to Figure 3A.

(B) H3K27ac ChIP-seq profiles at *Foxa1* and *Gata5* loci in N, P, T and M organoids.

(C) RNA-seq based *Foxa2* mRNA expression in organoids. Each dot represents an independent organoid culture, and the mean \pm SEM is shown. *p* value was determined by Student's *t* test.

(D) Metagene representation of the mean FOXA1 ChIP-seq signal at ALL regions in the indicated organoids.

(E) qRT-PCR of FOXA1 mRNA expression in human normal organoids (n = 3) and patient-derived PDA organoids (n = 21). The mean \pm SEM is shown. *p* values were determined by Student's *t* test.

(F-G) Representative immunohistochemistry (IHC) staining of anti-FOXA1 antibody and semiquantitative analysis of FOXA1 staining intensity in human normal pancreas (F, n = 5), PDA primary tumors (n = 35) and metastases (n = 38; 36 liver, 1 small bowel and 1 diaphragm) tissue microarrays and sections from Rapid Autopsy Program (G). FOXA1 nuclear staining intensity is classified into negative, weak, moderate and strong. The insets show a higher magnification of the indicated area. Scale bars, 100 μ m.

(H) Table shows GSEA summary for assessing differential enrichment of *GAIN* genes in the indicated stages of primitive gut tube differentiation from hES.

(I) Metagene representation of H3K27ac signal at *GAIN* regions during foregut differentiation of hES cells.

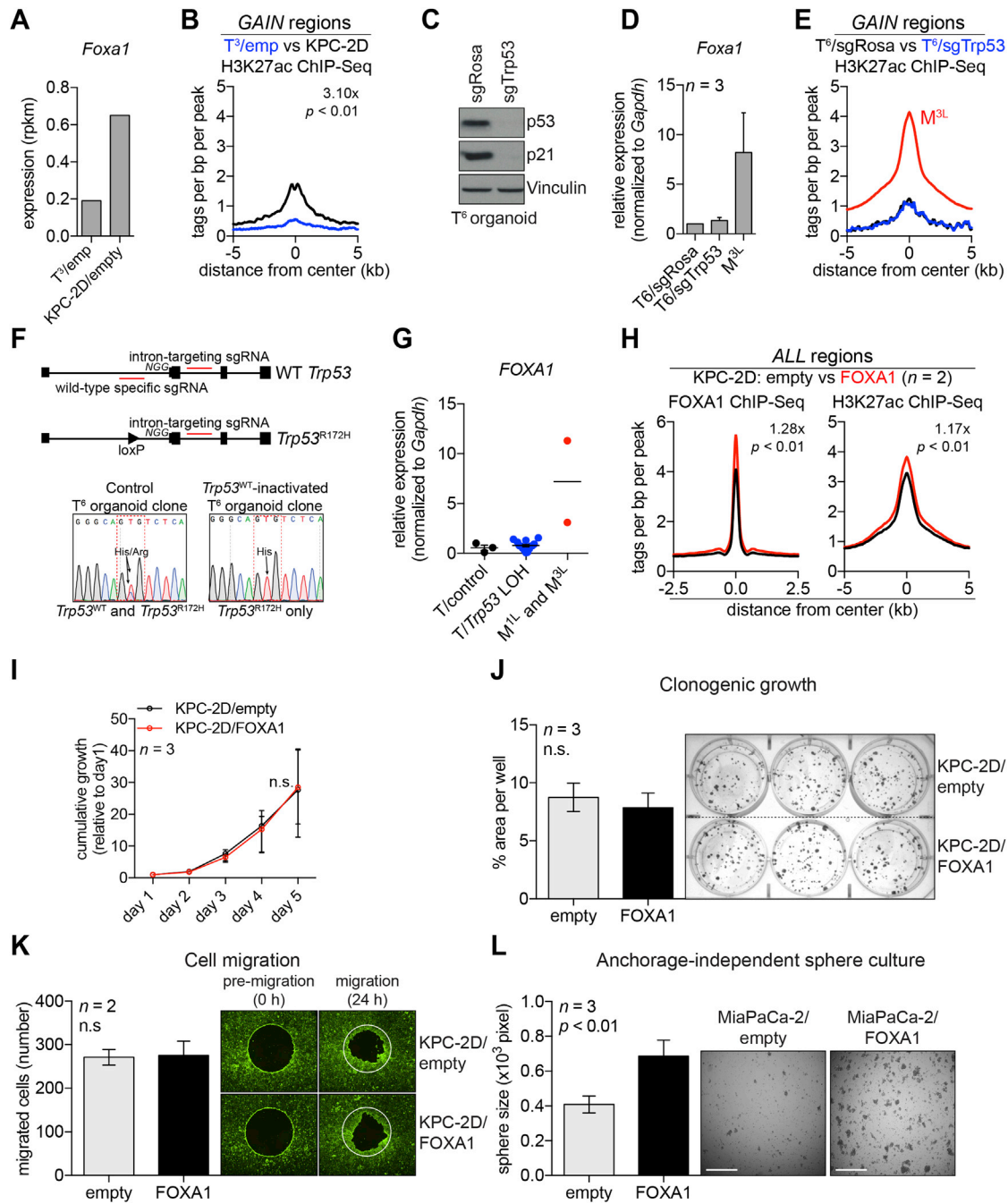


Figure S4. FOXA1 Occupancy and Its Role in Metastatic Capabilities of Murine and Human PDA Cell Lines, Related to Figure 4

(A) Representation of RNA-seq based *Foxa1* expression in T^3 /empty organoid or KPC-2D/empty cells.
 (B) Metagene representation of the mean H3K27ac ChIP-seq signal across *GAIN* regions in T^3 organoid and KPC-2D/empty cells.
 (C-D) western blot (C) and qRT-PCR analysis (D) of *Foxa1* expression in T^6 organoid with *Trp53* loss.
 (E) Metagene representation of H3K27ac signal of T^6 /sgRosa, T^6 /sgTrp53 and M^{3L} organoids at *GAIN* regions.
 (F) *Trp53* WT allele specific inactivation strategy using two gRNAs and representative chromatograms of *Trp53* cDNA Sanger sequencing at R172H region in T^6 organoid clones with *Trp53* LOH.
 (G) qRT-PCR analysis of *Foxa1* expression in clonally derived *Trp53* LOH clones ($n = 14$).
 (H) Metagene representation of the mean *FOXA1* (left) or H3K27ac (right) ChIP-seq signal across ALL regions in KPC-2D/empty and KPC-2D/*FOXA1* cells.
 (I) The cumulative proliferation of KPC-2D/empty and KPC-2D/*FOXA1* cells ($n = 3$). The number of viable cells was counted by trypan blue exclusion. The mean \pm SEM is shown and p value was determined by Student's t test.

(legend continued on next page)

(J) Clonogenic growth assay of KPC-2D/empty and KPC-2D/FOXA1 cells. One week after plating, colonies were stained with crystal violet to visualize and quantify clonogenic growth of KPC-2D cells.

(K) Exclusion zone based cell migration assay of KPC-2D/empty and KPC-2D/FOXA1 cells.

(L) Anchorage-independent sphere formation assay of MiaPaCa-2/empty and MiaPaCa-2/FOXA1 cells ($n = 3$). Bright field images were taken from 4x field after 2 weeks of culture and the size of spheres were measured for quantification. The mean \pm SEM is shown and p value was determined by Student's t test. Scale bars, 500 μm .

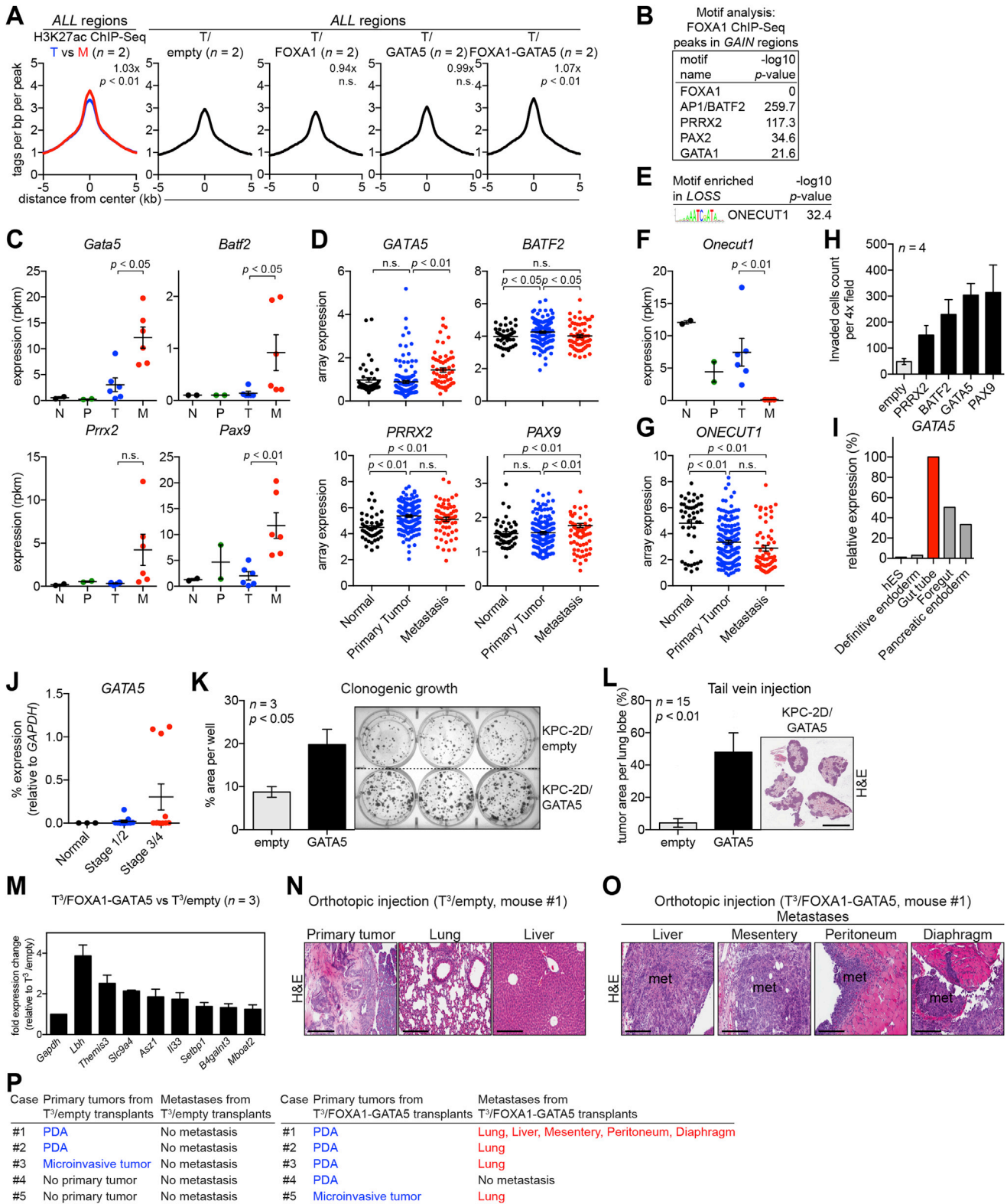


Figure S5. Potential Regulatory TFs in PDA Metastasis, Related to Figure 5

(A) Metagene representation of the mean H3K27ac ChIP-seq signal across ALL regions in indicated organoids.
 (B) TF motifs identified from 1,403 FOXA1 ChIP-seq peaks at GAIN regions.

(legend continued on next page)

(C and D) RNA-seq or microarray based *GATA5*, *BATF2*, *PRRX2* and *PAX9* mRNA expression in normal and neoplastic murine pancreatic organoids (C) or human PDA tumors (D), respectively. The mean \pm SEM is shown. *p* value was determined by Student's *t* test.

(E) Enrichment of *ONECUT1* motif in *LOSS* regions.

(F and G) RNA-seq or microarray based *ONECUT1* mRNA expression in murine normal and neoplastic pancreatic organoids (F) or human PDA tumors (G). The mean \pm SEM is shown. *p* value was determined by Student's *t* test.

(H) Boyden-chamber invasion assay of KPC-2D/empty, *BATF2*, *GATA5*, *PRRX2* and *PAX9* cells (*n* = 4 each). The mean \pm SEM is shown and *p* value was determined by Student's *t* test. Scale bars, 500 μ m.

(I) *GATA5* expression during pancreatic differentiation of hES relative to gut tube stage.

(J) qRT-PCR analysis of *GATA5* expression in human normal (*n* = 3) and patient-derived PDA organoids (*n* = 21).

(K) Clonogenic growth assay of KPC-2D/empty and KPC-2D/*GATA5* cells. One week after plating, colonies were stained with crystal violet to visualize and quantify clonogenic growth of KPC-2D cells.

(L) Tail vein injection of KPC-2D/empty and KPC-2D/*GATA5* cells (2.5×10^5 cells) into C57BL/6J mice to assess lung colonization at 4 weeks post-injection. Representative images of H&E staining are shown (right). Percent tumor area per lung lobe (%) was determined by dividing the whole surface area of the largest lung lobe with lung tumor area of the given lobe. The mean \pm SEM is shown and *p* value was determined by Student's *t* test (*n* = 15).

(M) qRT-PCR validation of *GAIN* genes for a comparison of T^3 /empty versus T^3 /FOXA1-*GATA5* (averaged from three biological replicates).

(N and O) Representative images of H&E staining of orthotopic injections of T^3 /empty and T^3 /FOXA1-*GATA5* organoids. Scale bars, 100 μ m.

(P) Summary of orthotopic injections of T^3 /empty and T^3 /FOXA1-*GATA5* organoids.

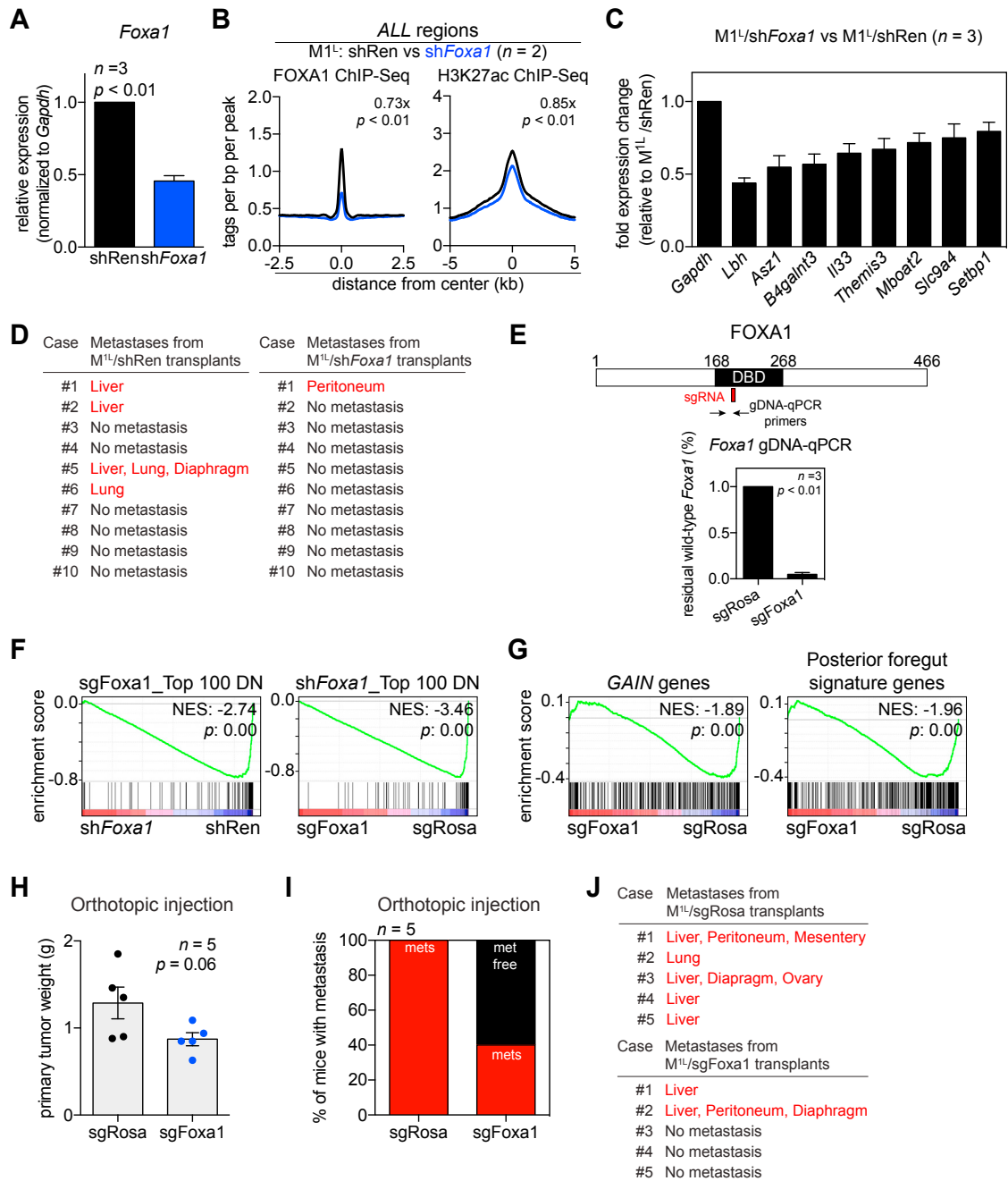


Figure S6. Effect of FOXA1 Suppression on Enhancer Landscape and PDA Progression, Related to Figure 6

(A) qRT-PCR analysis of *Foxa1* mRNA in M1^L/shRen or M1^L/shFoxa1 ($n=3$). The mean \pm SEM is shown. p value was determined by Student's t test.

(B) Metagene representation of the mean FOXA1 (left) or H3K27ac (right) ChIP-seq signal across ALL regions in the indicated organoids.

(C) qRT-PCR validation of GAIN genes for a comparison of M1^L/shRen versus M1^L/shFoxa1 (averaged from three biological replicates).

(D) Summary of distant organ metastasis upon orthotopic injections of M/shRen or M/shFoxa1 ($n=10$).

(E) CRISPR strategy targeting DNA-binding domain (DBD) of FOXA1 and qPCR validation of editing efficiency.

(F) GSEA of M1^L/shFoxa1 versus M1^L/sgFoxa1 using each top 100 downregulated genes.

(G) GSEA of M1^L/sgFoxa1 versus M1^L/sgRosa using GAIN genes (left), or posterior foregut signature genes (right).

(H) Quantification of primary tumor weight from injection site (pancreas) after orthotopic injection of M/sgRosa or M/sgFoxa1 organoids in athymic nu/nu mice ($n=5$). 5×10^6 cells were orthotopically injected and mice were sacrificed at 4 weeks post-injection. Each dot represents a mouse and the mean \pm SEM is shown. p value was determined by Student's t test.

(I) Quantification of the number of mice bearing metastases upon orthotopic injection of M/sgRosa or M/sgFoxa1 organoids ($n=5$).

(J) Summary of orthotopic injections of M1^L/sgRosa and M1^L/sgFoxa1 organoids.